UCLouvain

École polytechnique de Louvain

Design of a radar in order to detect debris in the GEO

Author: **François KOLLMANN**
Supervisor: **Christophe CRAEYE**
Readers: **Khaldoun EL KHALIFEH, Luc VANDENDORPE**
Academic year 2021–2022
Master [120] in Electro-mechanical Engineering

ACKNOWLEDGEMENTS

First and foremost I am extremely grateful to professor Craeye, who was always available to help me, and guided me well through this year of work. His knowledge and patience helped me immensely in my research and the writing of my thesis.
I thank Dr Philippe Morgand greatly who provided me precious advice and helped me in my task, and for sharing his vast knowledge about radars.
I would also like to thank Dr Khaldoun El Khalifeh for the very valuable guidance during the design of the antennas using the CST software.
Thanks to my family for their constant support through the year.
Finally, I would like to thank my friends for all the fun and the group work during these five years at university.

ABSTRACT

In this thesis, we design the base of a 5 GHz radar mounted on a satellite in order to detect debris in the geostationary orbit. The radar cross section of a cube the size of the wavelength is computed, its dependency on the frequency and angle of incidence are discussed. In order to scan the whole GEO, the radar flies on an orbit 150 km under the GEO, and has a steerable beam thanks to beamforming using an array of antennas. A constant value is found in order to approximate the RCS of a plate with a size close to the wavelength, as well as an analytical approximation of the RCS at lower frequencies and a curve fitting for higher frequencies. A design of a patch antenna array with a squared cosine distribution for the width of the patch is proposed, with a maximum gain of 30.3 dBi. An analysis of the SNR of the radar shows that the cube is visible on average up to 90km, and the radar is capable of detecting until the end of the GEO at a distance of 350 km objects with a RCS equivalent or greater than a sphere with a radius of 1m.

CONTENTS

CHAPTER 1

INTRODUCTION

On november 15, 2021, Russia tested its Anti-Satellite (ASAT) system by destroying an inactive russian satellite, the COSMOS 1408. The destruction of the satellite created thousands of debris. A few others countries such as the U.S.A., China or India have also tested their ASAT weapons in the last decades and by doing so have created a large number of debris of various sizes.

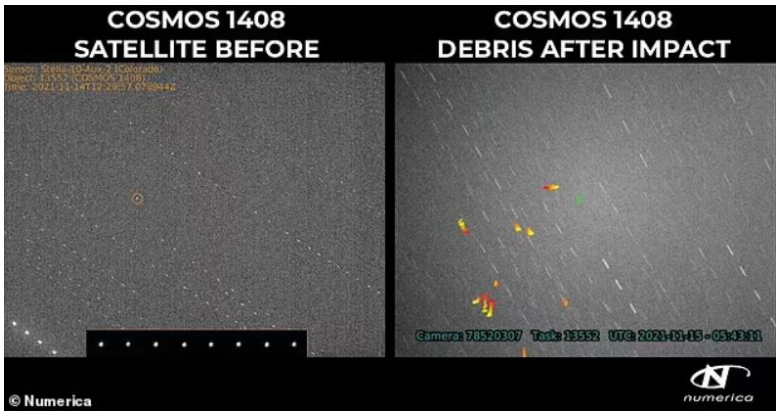

Figure 1.1: Before and after pictures of the COSMOS 1408 satellite's destruction. Some of the visible debris are highlighted in yellow and red in the second picture. Image from *DailyMail* [1]

But ASAT tests are not the only source of debris in space. More and more rockets are launched into space and their first stages stay in orbit, some satellites stay in their orbit after reaching the end of their life, while others get destroyed from collisions, creating even more debris. This is turning into a real problem as the risk of collisions grows with the number of debris in space. If nothing is done to at least slow down the buildup of space debris, it might soon be impossible to launch rockets into space due to the Kessler syndrome, a phenomenon where collisions become unavoidable, and satellites hit by debris shatter in many pieces, creating more and more debris. This creates a cascade of collisions, saturating the orbits around Earth with high-velocity debris, thus obstructing the launch of rockets and the use of the space altogether.

Recently, the European Space Agency released their annual Space Environment report [2], describing numerous statistics about debris, launches, and satellites counts in the different orbits. Since 2016, the formation of large satellite constellations - such as SpaceX's Starlink and later Amazon's project Kuiper - has highly increased the number of payloads being launched in space, especially in the Low Earth Orbit. In the geostationary orbit, while the ESA reported a

decrease in payload traffic in the last two years (Figure 1.2), the number of objects catalogued is continuing to increase, showing no sign of decline, with a sharp increase in the mid 2010s (Figure 1.3).

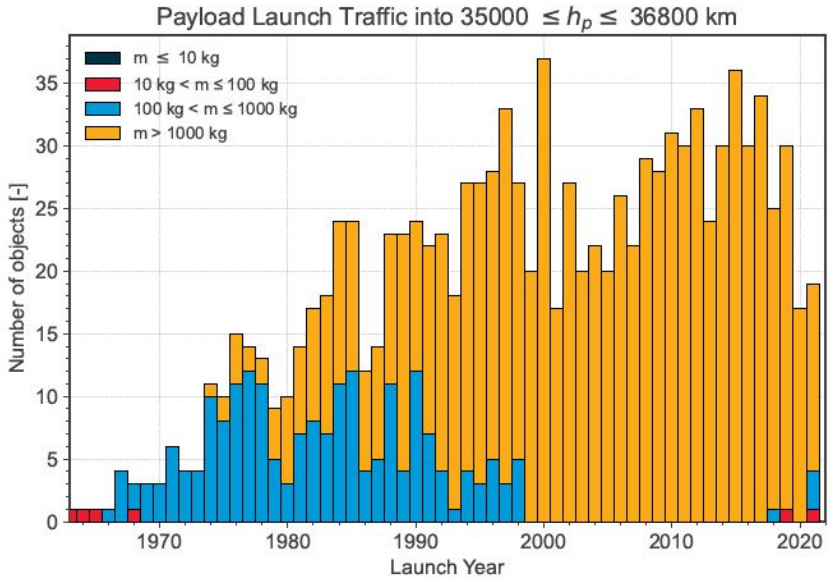

Figure 1.2: Payload launch traffic in the GEO. There has been a decrease in 2020 and 2021. Image from [2]

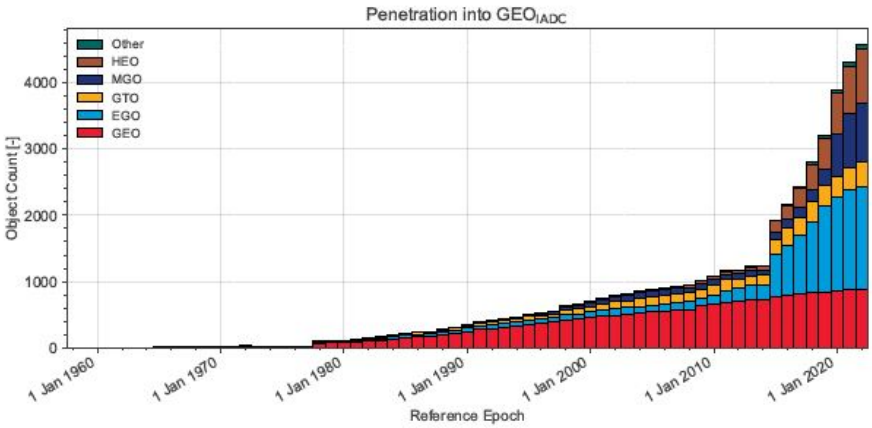

Figure 1.3: absolute number of catalogued objects that penetrated or resided in the IADC-protected GEO orbits. Image from [2]

Many debris in space are already being tracked and their trajectories are known, in order to find and remove them once we have the capability to do so. Meanwhile tracking them allows the ISS and satellites to maneuver in order to avoid them. Most of the tracked debris are in the LEO, as they can be seen and detected by the telescopes and radars on Earth. In the GEO however, the debris are much farther from the ground, making it much more difficult to detect from the Earth and no satellite-mounted radars exist to track them, as far as we know.

The report from the ESA indicates that approximately 30 thousand objects are tracked in space, with more than 20 thousand in the Low Earth Orbit, and less than 5 thousand in the geostationary orbits. While inferior than at the Lower Earth Orbit, the density of debris in the geostationary orbit should be tackled as early as possible to ease the clean-up and diminish any

potential risk. A study done by the ESA reports that it would be 25% less effective to start removing space debris in 2060 than to start now.

Debris mitigation

The effort to decrease space debris creation begun in the mid 1990s. The first guidelines for debris mitigation were written in 1995 by NASA. The following years, other space agencies followed NASA by publishing their own guidelines, until 2002 when the Inter-Agency Space Debris Coordination Committee (IADC) of which 12 countries and ESA are now part released a set of guidelines in order to control the increase of debris in space.
In 2007, a new consensus of guidelines was designed using the previous ones as a base, and the United Nations adopted it. 63 members of the United Nations now follow voluntarily these ground rules in order to lessen the growth of debris in space.

Nowadays, ESA follows the ISO standard 24113 [3] on debris mitigation requirements. The main topics of the guidelines concern the disposal of satellites once they have completed their mission, reached their planned end-of-life or have been damaged and are unable to function properly anymore.
Citing the ISO standard document, the main goals of following these standards are :
“

a) avoiding the intentional release of space debris into Earth orbit during normal operations;

b) avoiding break-ups in Earth orbit;

c) removing spacecraft and launch vehicle orbital stages from protected orbital regions after the end of mission;

d) performing the necessary actions to minimize the risk of collision with other space objects;

e) reducing the risks associated with re-entry, e.g. to people, property and the Earth's environment.

Such actions are especially important for a spacecraft or launch vehicle orbital stage that has one or more of the following characteristics:

– has a large collision cross-section;

– remains in orbit for many years;

– operates near manned mission orbital regions;

– operates in highly utilized regions, such as protected regions;

– operates in regions of high debris population.

”

In practice, the satellites have techniques to remove themselves from their orbit.

At the Low Earth Orbit, they are expected to de-orbit and reenter the atmosphere of the Earth in order to burn up, within 25 years after the end of their mission.

At the Geosynchronous orbit, rockets' parts and satellites cannot reenter the atmosphere so they must move to a graveyard orbit, 300 km further than the GEO belt, to make place for future other satellites and be sure that the defunct ones do not collide with others, destroying them and creating a large number of debris at the same time.

Before proceeding to the disposal of the satellite, it must go through passivation, that is the emptying of its energy reservoirs, be it electricity stored in batteries, fuel or pressurant. This is done to avoid any risk of explosion once the satellite is decommissioned.

Even with these guidelines and standards implemented, there is a need to improve the safety of operations in space. The ESA enacted in 2009 the Space Situational Awareness [4]. The SSA programme is split in three parts :

- **Space Weather** : observing and predicting the continuous changes around Earth such as in the ionosphere, magnetosphere, thermosphere as well as the Sun's activity. These can have an effect on the infrastructure in Earth and in orbit, and need to be monitored in order to respond accordingly to change that might cause problems and hurt.
- **Near-Earth Objects (NEO)** : detection of objects, for example asteroids coming close to the Earth and that could possibly impact it and cause harm.
- **Space Surveillance and Tracking (SST)** : surveillance of working and defunct satellites, as well as other objects such as debris, stages of a rocket, ...

The three items are being developed in parallel, in order to improve the security of satellites and humans, both on Earth and in space. This project allows Europe to have its own source of information about space conditions and to be independent from other nations.

The part that concerns us is the Space Surveillance and Tracking. At this level, the ESA works on developing and sharing new technologies in order to create an Europe-wide SST system, where the nationally-funded projects of member countries can share and use data from others easily and efficiently. Pooling together intelligence from the many countries in Europe allows for more precise information and in higher quantity. the SST programme thus helps satellite operators to react faster and more efficiently to threats.

In this thesis, a first design for a satellite-mounted radar to track debris in the geostationary orbit is proposed. Information about the environment of the radar are given, as well as details about the working principles of the radar. An analysis of the response of a simplified debris is carried out. A proposed antenna design and specifications are shown and finally, the capabilities and limitations of the radar are computed and discussed.

CHAPTER 2

LITERATURE REVIEW

The number of debris in space is a growing concern in the world. Several systems to track and catalogue them are being developed around the globe.
One of the most recent and powerful debris-tracking radar is the Space Fence from Lockheed Martin [5]. Operational since end of March 2020 in the USA, it can detect objects of the order of a centimeter in the Low Earth orbit with an average radiated power of 0.81 MW from its array of 36000 antennas.

Figure 2.1: Space Fence Radar : the smaller off-white roof covers the emitting antennas while the larger one houses the receiving ones. The white poles help calibrate the radar. Image from [5]

While it is also capable of seeing objects on the Geostationary orbit, no order of magnitude has been given for the size of objects observable at that height.

In Germany, TIRA [6] (Tracking and Imaging RAdar) is a radar with a diameter of 34 m. Working since 1970 and recently renovated in 2014, TIRA has a high-power tracking radar working in the L-band and an imaging radar in the Ku-Band. Capable of high imaging resolution and depth resolution, it can provide precise information about space debris and satellites in space for evading maneuvers or high quality images of satellites.

Similar to TIRA, France also has a radar for space surveillance : GRAVES (Grand Réseau

Adapté à la Veille Spatiale) [7]. It is a bistatic radar working at 143.050 MHz, with the emitting and receiving antennas separated by 400km. It is able to detect the presence, absence or maneuvers of a satellite, as well as the arrival of a new satellite. It is capable of detection of microsatellites (a surface of at least a square meter) at range between 400 and 1000 km.

Not only radars are used to detect objects in space. The IZN-1 [8] is a laser ranging station developed and operated by ESA in Tenerife, Spain. Although it uses a 150 mW laser that can only detect and track satellite equipped with reflectors, it is planned to be upgraded with a 50 W laser in order to track debris as well. The facility will be used as a testbed for laser technologies that will nudge the smaller debris, in order to change their momentum, reorbit them and in doing so avoid collision with another object.

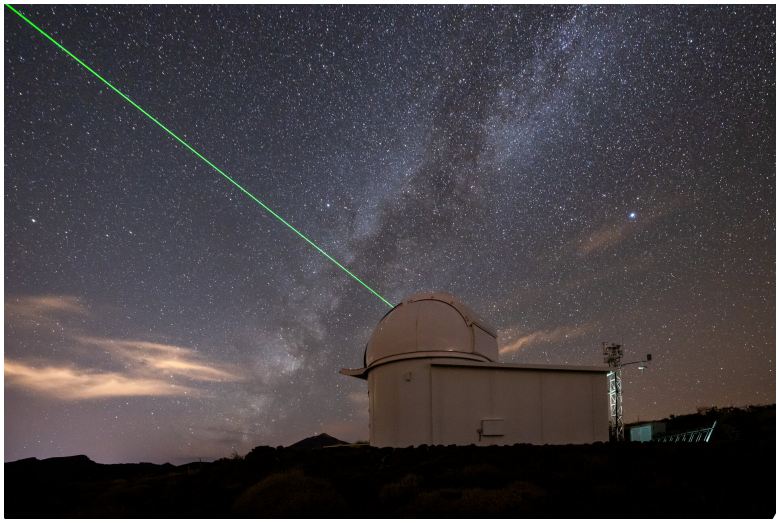

Figure 2.2: IZN-1 Laser ranging station. Image from [8]

Telescopes are also used to detect and track debris in space. The Space Surveillance Telescope [9] is an american military telescope that was first officially operated in 2011 in the USA. It is now in Australia since 2022 in order to survey the southern celestial hemisphere, tracking and cataloguing debris and satellites.

A Canadian microsatellite named NEOSSat (Near Earth Object Surveillance Satellite) surveys the inferior-to-Earth-orbit for asteroids using a telescope. The suitcase-sized satellite is capable of detecting asteroids. These asteroids orbiting the sun are otherwise invisible from Earth since they appear in the sky during the day, and are masked from the telescopes by the sunlight.

D-Orbit has a satellite launch service called InOrbit Now (ION). It provides Satellite Carrier Vessels to its customers in order to set their satellites ready to work optimally and as fast as possible. These carriers are fitted with various equipment and sensors for them to carry out their task successfully. D-Orbit repurposed this infrastructure already in space for Space Surveillance and Tracking (SST) [10]. They now can observe debris and satellites using the multiples star tracker cameras present on the satellite carrier. The project is still improving but highlights the possibility to reuse existing hardware in space once its main purpose has been achieved.

2.1 Removing debris

Once a debris or a defunct satellite is tracked, its removal can be set forth. For this task, multiple strategies have been proposed over time :

TugSat [11]

Proposed by the University of Florida in Gainesville, Florida, TugSat develops on the idea of using a solar sail to move the satellite and its captured debris out of the geosynchronous orbit. Once they are out of the higher bound of the orbit, the debris is released from the grasp of the reorbiter, which can start its maneuver to come back to the GEO and start its operation on a new debris.
TugSat does not offer a way to grab or connect to a debris, but a distinct propulsion system that does not need any fuel but only the solar radiation pressure.
The simulation with a 1000 kg debris removal highlights the possibility of using solar sails for the clearing of large objects in the GEO, the re-orbiting and the return to the orbit done in less than two years.

Reorbiter using ion beam radiation [12]

Hosei University in Tokyo, Japan, has proposed to remove large debris in the GEO using ion beam radiation. The design of the satellite includes two ion engines on opposite faces. One would fire its ion beam on the debris to give it momentum, and the second one is controlled for the reorbiter to follow its target debris. The satellite would thus push the debris out of the geosynchronous orbit, into a cemetery orbit, 300 km above. It then comes back to the GEO to process another debris. An estimation of the time taken to remove debris was done and the outcome shows that six debris can be moved out of the orbit in 170 days.
The advantages of this system is the absence of contact between the target and the satellite : the shape, size and rotation of the debris will not prevent the satellite from re-orbiting it.
The challenges facing this project for now is the beam convergence necessary to produce an efficient debris irradiation, with computations and basic experiments reporting a feasibility of the needed irradiation efficiency (ratio between thrust to the debris and the total thrust of the ion engines) around 25%.

Space Sweeper with Sling-Sat [13]

This theoretical satellite would use plastic collision during the capture to remove the debris. The satellite would exploit these collision by using the gained momentum from it in order to reduce its consumption of fuel. They computed a decrease of 40% of fuel use than a more conventional satellite that would need to meet the debris close, capture it and repeat. This satellite would require its structure and materials to be capable of enduring multiple collisions without breaking apart.

Astroscale's ELSA [14]

ELSA stands for End-of-Life Services by Astroscale. The company is currently demonstrating its solution for defunct satellites and debris removal, using a satellite that connects employing a magnetic docking mechanism. Its plan of action is to rendezvous closely with the target, extend its magnetic docking system and connect with the debris. Once connected, the deorbiting phase begins and the pair descends into the atmosphere to burn up.
During the concept demonstration, Astroscale hopes to prove its satellite's capability to dock

with both a non-tumbling and a tumbling debris, as well as discovering and meeting up with a far away target.

SJ-21 [15]

On January 22 of this year, a Chinese satellite, the SJ-21 has been seen docking to an inactive satellite and sending it out of the geostationary orbit (and beyond the cemetery orbit, where the satellite at the end of their life are sent). After the maneuver, the SJ-21 returned to the geostationary orbit. While China has not communicated about the event, it shows that the feat is achievable.

ClearSpace-1 [16]

ClearSpace-1 is the first debris-removal mission of ESA, directed by ClearSpace SA, a spin-off from the EPFL, the Ecole Polytechnique Fédéral de Lausanne, in Switzerland. Planned to be launched in 2026, it aims to remove a debris of 112 kg, the Vespa upper stage from the Vega launcher. Its action plan is to meet with the debris, catch it with 4 robotic arms developed by ESA and then descend into the atmosphere where both safely disintegrate.

CHAPTER 3

ENVIRONMENT DEFINITION

Before detailing the numerous parameters dimensioning the radar, we must define the environment in which it will operate, as it has a significant impact on its design and its capabilities.

3.1 Orbit of the satellite

We need to find a way to scan the whole geostationary orbit, which goes all around the Earth. Philippe Morgand proposed an efficient solution of setting the satellite on a different orbit than the one we are trying to scan, allowing the radar to move at a different speed and thus to comb the GEO without the use of an active propulsion system. We have to decide the orbit on which the satellite will be flying. This will have multiple influences, notably on the capabilities of the radar, as well as the positions of the debris it will be able to see and the time it will take to survey the whole geosynchronous orbit.

The orbital speed is given by the equation

$$v \approx \sqrt{\frac{GM}{r}} \tag{3.1}$$

where we have

- the universal constant of gravitation $G = 6.674 * 10^{-11}[m^3 kg^{-1} s^{-2}]$
- the Earth's mass $M = 5.972 * 10^{24}[kg]$
- the distance from the center of the Earth r.

The geostationary orbit is situated 35 786 km above Earth, which gives $r \approx 42000$ km, and thus a speed of around 3080 m/s.
Since we wish to survey this orbit, we cannot go at the same speed. We need to find an orbit where the relative speed would allow us to survey the entire orbit in an acceptable period. An orbit 150 km lower than the GEO was proposed, this gives a speed of approximately 3086 m/s, or a speed of 6 m/s relative to the GEO.
The orbital period of a satellite is given by

$$T = \frac{2\pi r}{v} \tag{3.2}$$

We deduce that it would take 507 days or 1.39 years to survey the whole geostationary orbit, which is adequate for the scale of the mission of our satellite.

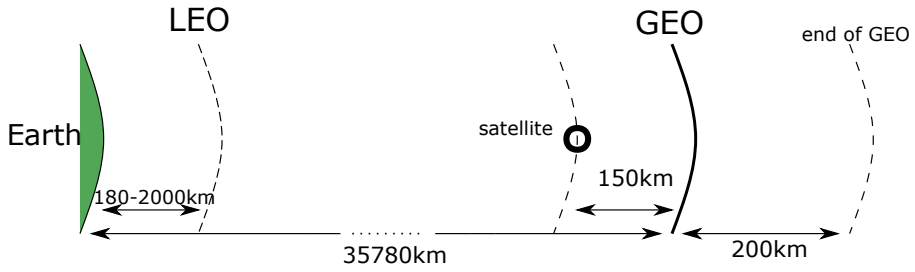

Figure 3.1: illustration of the different orbits

3.2 Power management

The satellite will get its power from the sun using solar panels. But during each revolution around the Earth, the satellite will be in the shadow of the Earth. During this time, the solar panels won't be able to capture the sun's power and the satellite will have to rely on batteries. It is important to take all this into account since the power we are able to provide to the radar will impact directly the detection of objects.

First of all, the sun light irradiance at the outer atmosphere is around 1373 kW/m^2, distributed among different wavelengths of the light, as is illustrated on the graph in Figure 3.2. In space, since energy production is very limited, the solar cells used are triple junction solar cells that can use 3 different frequency bands to generate electricity. They are costlier than single or double junctions but more efficient. This is a significant advantage when the size of the solar panels is limited, in our case by the payload of the rocket that will launch the satellite to space.

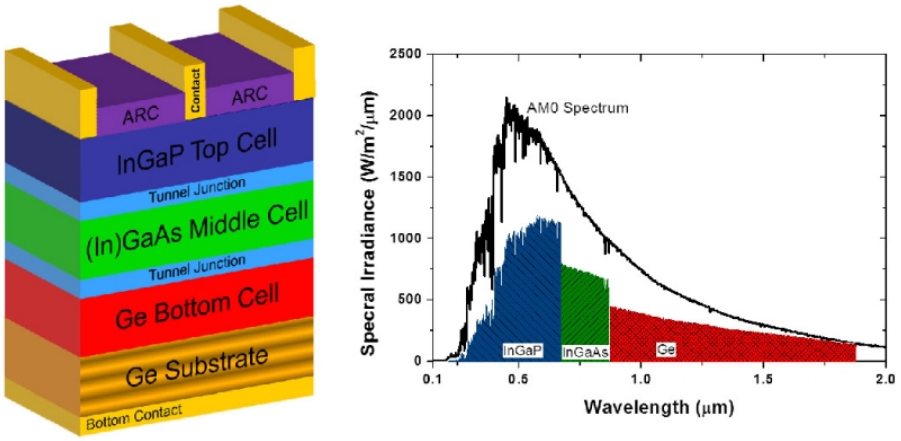

Figure 3.2: triple junction cell and the wavelength bands it absorbs. Image from Spie.org [17]

The efficiency of solar panels decreases during their lifetime. Concerning the technology of the triple-junction solar cells, the efficiency at Beginning of Life (BoL) is around 40%, and will decrease down to 15 to 20% at their end of life. This means that in an optimal situation, the solar panels would generate 549 W/m^2, and down to 275 W/m^2 if the efficiency drops to 20% at the end of life.

Since there is a lack of information regarding the efficiency decline of solar panels in space, corresponding data for Earth-based solar panels is used. A study on the degradation of photovoltaic panels[18] published in 2011 reported an average decrease of 0.8% of its initial efficiency per year, with a drop between 1 and 3 % during the first year. For a solar panel to drop from 40% to 20% would take on average 61 years. We can expect the space environment to be harsher to the panels than Earth, and they might decay at a faster rate, but the satellite may cease functioning long before for other reasons.

Furthermore, as already mentioned, during each revolution, the satellite will be in the shadow of the Earth. At the geostationary orbit, that will last 1h30 out of the 24h. During this time, the solar panels will not be able to produce power. This implies the need for batteries as well as the necessity to charge them. This brings to light the interdependency of 3 important parameters of the satellite:

- the power that will be transferred to the radar
- the size of the batteries that will be required
- the surface of the solar panels.

We wish to send as much power as possible to the radar, but an increase in the power provided would demand not only a greater surface of solar panels but also bigger batteries, that will in turn increase the need for solar panels.
There is an optimal combination of parameters, but before dwelling on that issue, it is necessary to have an estimate of the power needed for the proper functioning of the radar.

In order to have an idea of the solar panel surface, as well as the battery size that will be needed, some comparisons have been made for different surfaces of solar panels as shown in Table 3.1.
Some assumptions were made to calculate those values :

- the efficiency of the solar panels is set to 20%, as if the solar panels were at their end of life. The power produced is thus of 275 W/m^2.
- an arbitrary distribution of power was chosen : 93.5% of the power from the solar panels would supply the satellite for it to function properly (the "Power to function" column of the table 3.1), while the rest would serve to charge the batteries.
- two types of batteries were taken as examples from a slideshow from Pr. M. Bekemans [19]. The first one is the NiH_2 battery with a capacity of 35-40 Wh per kg, while the second is the Li-ion battery with a capacity of 60-70 Wh/kg. The lower values were used during the calculations.

The energy capacity needed is the power needed to function times the duration the satellite is in the shadow of the Earth : 1h30 min. The energy to charge the battery is the spare 6.5% of the power from the solar panels that will charge the battery while the satellite is exposed to the sun; i.e. during 22h30 min.

Solar Panel Area	Total Power	Power to function	Power to charge batteries	Energy to charge batteries	Energy capacity needed	Battery weight 1	Battery weight 2
$[m^2]$	[W]	[W]	[W]	[Wh]	[Wh]	[kg]	[kg]
1	274.6	256.75	17.849	401.6	385.13	11	6.4188
2	549.2	513.5	35.698	803.2	770.25	22	12.838
3	823.8	770.25	53.547	1204.8	1155.4	33	19.256
4	1098.4	1027	71.396	1606.4	1540.5	44	25.675

Table 3.1: comparison of powers with different sizes of solar panels

The choice of 93.5-6.5 % for the power distribution was made trying to give around 500W to the radar using 2 m^2 of solar panels, but in restrospect, this only leaves around 13.5W for the rest of the satellite, which is deemed to be too low. However, the choice of 3 m^2 gives approximately 270W to power the rest of the electronics, which seems reasonable. Thus this choice of distribution might not be bad as a first estimate. A power of 500 W seems to be a reasonable value to power the radar, while being constrained by the size of the solar panels.

In perspective, studying the boundaries for the size of our satellite could be interesting; Having an idea of the order of magnitude for the total weight of the satellite and its associated launch would allow us to make better choice for the size of certain components.

CHAPTER 4

PULSE FREQUENCY-MODULATED RADAR

A radar works by sending an electromagnetic wave which gets reflected when it meets an object. Once the reflection comes back to the radar, the distance between the radar and the object is known using the simple equation

$$distance = \frac{\Delta T}{2c}$$

where ΔT is the time the wave took to go and come back and c is the speed of light.
If the wave is reflected on a moving object, the doppler shift can be observed by comparing the received wave to the emitted wave : all the frequencies will be shifted

$$f_r = f_t \frac{1 + v/c}{1 - v/c} = f_t \frac{c + v}{c - v} \tag{4.1}$$

with f_r the received frequency and f_t the emitted frequency, assuming a a velocity much smaller than the speed of light.
The Doppler shift is defined as

$$\Delta f = f_r - f_t = \frac{2v f_t}{c - v} \tag{4.2}$$

By comparing with an emitted wave, we can thus find the radial velocity v, that is the velocity at which the object is approaching or moving away from the radar.

Radars can be classified into two types : the continuous-wave and the pulse radars.

Continuous wave radars emit a signal at all times and can receive signals at the same time. To recognize an object's echo without ambiguity, that echo needs to come back while the pulse is still going; continuous wave radars are more suitable for short range detection.

Pulse radars send electromagnetic waves by intermittence : for a short time, the radar will emit. It will then wait for a period of time, allowing the emitted signal to reach a certain distance, designated as the maximum depth the radar can see, and then potentially come back. During this time, the radar receives any potential reflections on any object that might stand in the way of the emitted wave.

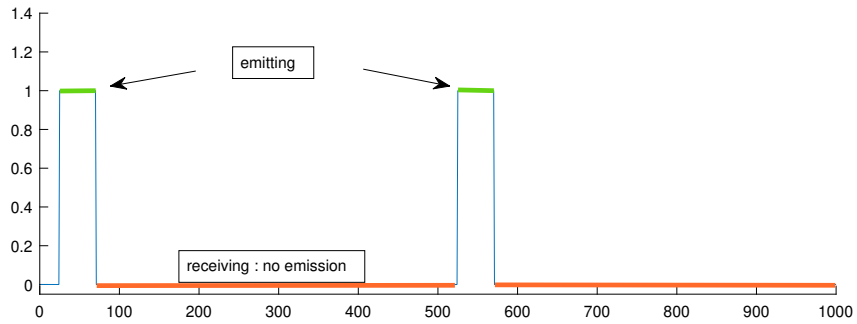

Figure 4.1: Illustration the duty cycle of a pulse radar

An important parameter of a pulse radar is the Pulse Repetition Interval (PRI). It is defined as the duration between two adjacent pulses. It is the sum of the length of a pulse and the time for this pulse to go as far as we wish to survey and to come back. In Figure 4.1, it corresponds to the sum of one green and one orange period.
It is expressed as

$$PRI = \frac{2\,D_{max}}{c} \tag{4.3}$$

where D_{max} is the largest distance from which the radar will be able to receive complete reflections from and c is the speed of light.

The duty cycle is simply the length of emission of one pulse over the PRI :

$$\text{duty cycle} = \frac{T_{pulse}}{PRI} \tag{4.4}$$

As the radar emits pulses of electromagnetic waves, its consumption of power is not continuous. It depends on the duty cycle as well as on the average power. It can be computed as :

$$P_{pulse} = \frac{P_{avg}}{\text{duty cycle}} \tag{4.5}$$

However, there is a limit on how much power can be sent by the radar and how often it can be emitted before the electronics overheats, and it is more demanding on the power amplifiers, which may start to behave non-linearly.

While a longer pulse allows sending more power and thus improves the capabilities of the radar, it comes with a trade-off. While the pulse radar is emitting, it cannot receive echos of its signals. The reason we cannot receive while we emit with a pulse radar while it is possible with a continuous-wave radar is the difference in power; the power of a pulse radar is much higher, creating stronger interference on the receiving antenna, or even saturating the amplifiers just behind.

We thus have blank zones where objects cannot be seen by the pulse radar. If a debris is in that blank zone, part the echo reflected on that object will reach the receiving antenna while the radar is still emitting. Passing that incomplete signal through the matched filter (explained in more details in section 7.2.1) will not yield a good result and the object has high chances to remain undetected by the radar.

The blank zone is given by the equation

$$D_{blank} = \frac{c\,T_{pulse}}{2} \tag{4.6}$$

For example, if we had a pulse of 1 ms, the blank zone would be of 150 km, a far too great zone. Given our orbital configuration (see Chapter 3.1), we consider that a reasonable blank zone could be 50 km long, making a pulse duration of 0.333 ms. The furthest we want to scan is 350 km from the radar, making the duty cycle of the radar 14.27%. If we supply the radar with an average power of 500 W as proposed earlier in Section 3.2, the actual power of the emitted pulse is 3500 W. This may be too demanding on the patch antennas from a thermal point of view, and it might be necessary to lower this value.

The signal sent by the radar is frequency-modulated; more precisely, the frequency is increasing linearly while being emitted. Figure 4.2 illustrates a frequency-modulated sine wave. The difference between the highest and lowest frequencies emitted by the radar is defined as the bandwidth B.

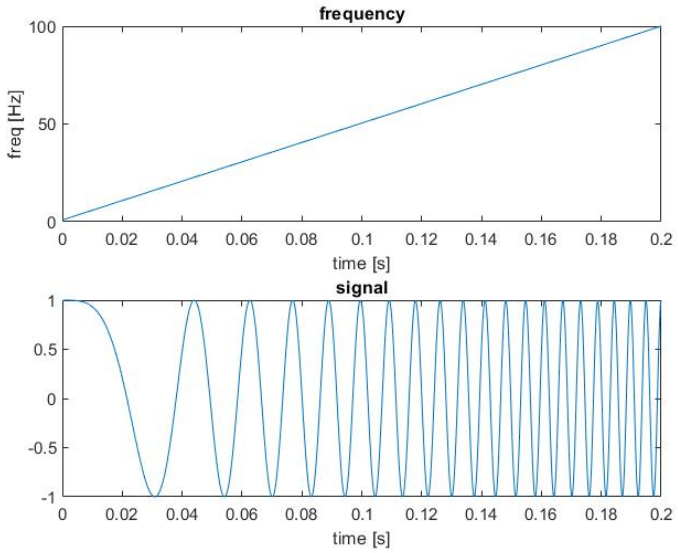

Figure 4.2: example of linearly increasing frequency sine wave

It is possible to further increase the distance for which we can process a received echo without ambiguities. By using a falling-frequency pulse after a rising-frequency one, we can distinguish two following pulses and thus double the distance that can be scanned without ambiguity. However, with the distance increasing, so do the propagation losses. This means that while we can actually receive the echos from objects further away, they will be harder to detect. Also, since the radar is emitting again, another blank zone will be created in the extended scanned zone.

There is another characteristic of the radar that limits our ability to observe objects without ambiguities : the sampling rate of the ADC. The sampling frequency of the ADC must respect the Nyquist-Shannon sampling theorem, citing the need for the sampling frequency to be at least twice the bandwidth of the signal it is sampling to ensure that no information of the signal is lost.
The signal does not need to be sampled at extremely high rates if the radar signal is in the GHz, since correlation can also be carried out in analog form using a matched filter.

4.1 Scan of the orbit

The volume we wish to scan using the radar has the shape of a torus around the Earth (Fig 4.3). There are three dimensions to take care of in order to scan this volume : the depth, the horizontal and the vertical dimension of the torus.

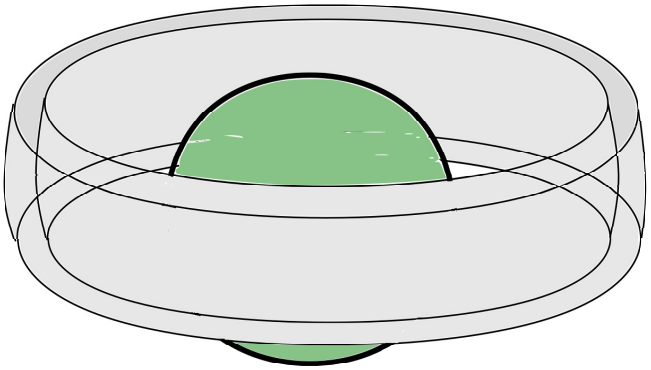

Figure 4.3: illustration of the torus representing the GEO belt around the Earth

A segment of this torus is represented in figure 4.4. The orbit of our satellite-mounted radar is a circle in the middle of the torus, 50km from the inner radius.

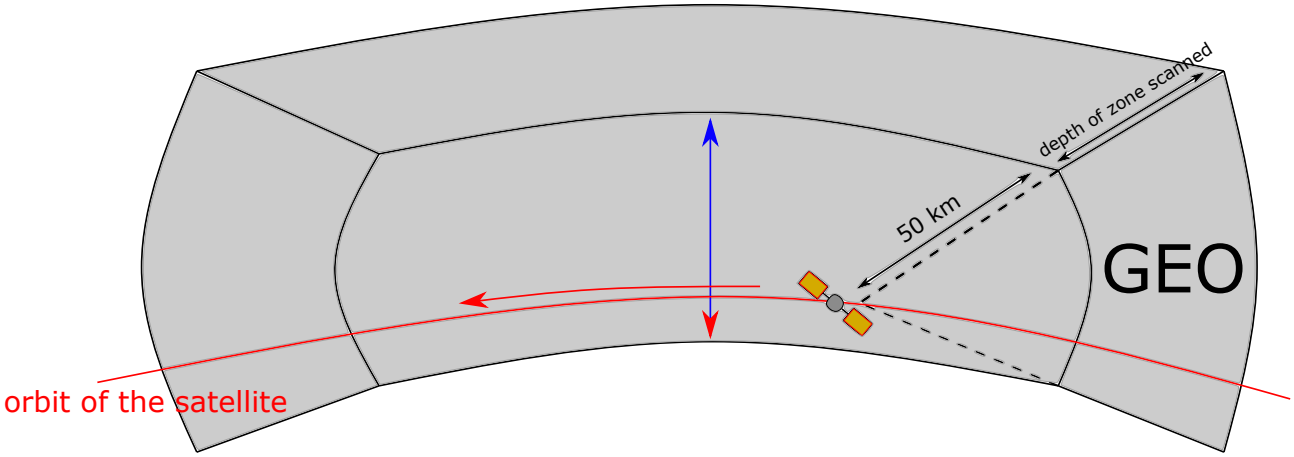

Figure 4.4: illustration of a section of the GEO belt

The dimensions can be processed independently from each other.

4.1.1 Depth scan

The depth scan is done by sending a pulse and then waiting for the echo, and calculating the distance of the object considering the time it took for the reflection to come back, as it has already been explained earlier. A higher accuracy is achieved by introducing a linear frequency modulation in the transmitted signal : the correlation with an equally modulated reference signal then produces a sharper peak, with a width inversely proportional to the used bandwidth (pulse compression, explained in more detail in Section 7.2.1).

4.1.2 Horizontal scan

The "horizontal" here is defined as the direction along the orbital line. As the orbit is lower than the middle of the geostationary orbit's depth, the satellite will not move at the same speed,

as detailed in section 3.1. The horizontal scan of the GEO is thus done 'independently' of the radar, since the satellite simply orbits at a different speed than the GEO, and will therefore change naturally the horizontal section of the orbit scanned. A sufficiently narrow radiation pattern in that direction allows distinguishing targets along the orbital path. The imaging could be improved through SAR processing [20] where a virtual array much greater in size than the physical array can be formed as the radar flies on the orbit.

4.1.3 Vertical scan

Vertical here is defined as the perpendicular direction to the orbital path. From the design of the antenna in Section 6, the mainbeam of a single antenna is $\gamma = 7.8°$ large and $\beta = 75.9°$ wide. The angle β is meant to be aligned vertically, the same direction in which the beamforming will be done. Horizontally, the cell resolution is set with the angle γ and increases with distance d with the relation

$$R_{horizontal} = \gamma \cdot d \tag{4.7}$$

At 50 km, this results in a resolution of $R = 6.8$ km. However, for the vertical resolution, we cannot keep such a large beam, as it would prevent

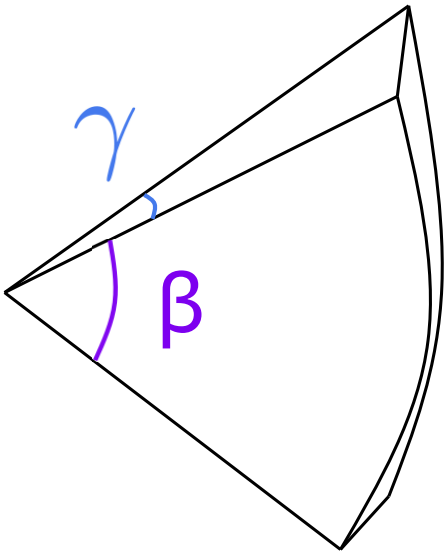

differentiating between a debris in the higher part of the belt and one in the lower part. So beamforming is introduced. According to the distance between the antennas and the phase shifts imposed to signals to and from each antenna, zones of constructive and destructive waves are formed, allowing us to make our beam directive only in a precise direction.

Beamforming is an extremely useful technology used in antennas and radars. By using an array of antennas and adjusting the phase of the signal sent or received separately at each antenna, it is possible to analyse data that could not be observable otherwise. Digitally modifying the phase of the signals received at every antenna accordingly (in other words adding delay to the signals) allows one to add up the signals as if they were all constructive for a specific direction (representation in Fig 4.5).

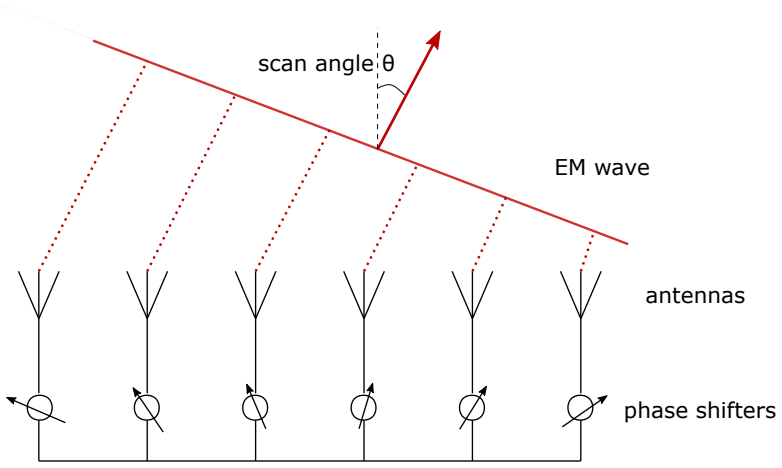

Figure 4.5: beamforming : in order to receive a signal from an angle θ, the antennas undergo different phase shifts before being added.

The total radiation pattern is the sum of the ones of each antenna of the array considering their respective phase shifts and possible amplitude weights. Depending on the positioning of the antenna in the array, the signals from the antenna exhibit a physical phase shift compared to one of the antenna used as a reference. Another phase shift can be implemented in the processing of the signal, which is not dependent on the position of the antennas but is arbitrarily imposed by the user.

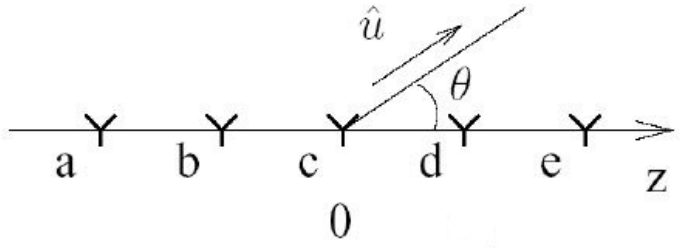

Figure 4.6: linear array along the z axis. Space evenly by a distance d, the antenna c is taken as reference. Image from [21]

This influence of the array can be computed using the following formulas :

$$\vec{F}(\vec{u}) = \sum_n \vec{F}_{no}(\vec{u})\, exp(jk\vec{\rho}_n \cdot \vec{u}) \tag{4.8}$$

$$= \vec{F}_o(\vec{u}) \sum_n a_n\, exp(jk\vec{\rho}_n \cdot \vec{u}) \tag{4.9}$$

$$= \vec{F}_o(\vec{u}) \sum_n A_n\, exp(jk\vec{\rho}_n \cdot \vec{u})\, exp(j\alpha_n) \tag{4.10}$$

$$= \vec{F}_o(\vec{u})\, R(\vec{u}) \tag{4.11}$$

We suppose every antenna are the same, thus, in first approximation, they all have the same individual radiation pattern $\vec{F}_o(\vec{u})$. The vector $\vec{\rho}_n$ represents the direction and distance of the n-th antenna with respect to the reference antenna (the choice of this reference is arbitrary). The term a_n is a complex coefficient set by the engineer designing the array. This term can be divided into two coefficients : $exp(j\alpha_n)$ is the phase factor of the n-th antenna with respect to a reference antenna while A_n is the weight of the n-th antenna, giving it more or less significance than other antennas in the array. $R(\vec{u})$ is named the array factor.

In our case, we have a linear array, such as the one shown in Figure 4.6, but with more antennas. The array factor is written as

$$R(\theta) = \sum_n A_n\, exp(jkz_n\, cos\theta)\, exp(jn\alpha) \tag{4.12}$$

The arbitrary phase shift has been set to be linear, increasing by α with each antenna. The phase shift that depends on the placement of the antennas varies linearly too, proportionally to a factor z_n which are the distances between a given antenna and the reference one. The cosine factor depending on θ defines a projection that produces the different distances of propagation, with θ angle we are sending or receiving a signal from.
In order to preserve a high sensitivity, we do not modify the amplitude distribution of the currents between the antennas (A_n), and only manipulate the phase change due to the spacing between the antennas (positions z_n) and the arbitrary phase change in post-processing (α).

It is also possible to illustrate this array factor as shown in figure 4.7:

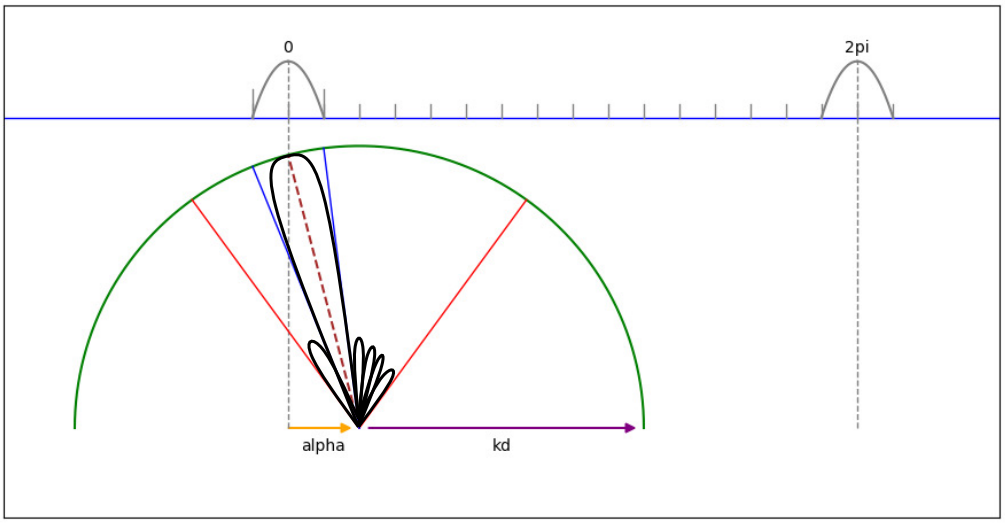

Figure 4.7: illustration of the far field resulting from beamforming with d = 0.03 m. The brown dotted line represents the direction of the main beam after beamforming, its width is defined by the blue lines. The red lines represent the limit of the original beamwidth. Past these lines, the magnitude of the radiation is much lower and is neglected.

The radius is defined by the product *kd*. If the distance d between the antennas is too large, grating lobes (parasite lobes as high as the main lobe) will appear, but increasing the distance also reduces the width of the main beam, making the array more directive and improving the cell resolution of the radar. The arbitrary delay α that we set between the antennas moves the center of the half circle right or left, allowing us to change the angle of the main beam.

From antenna array theory, the width of the main lobe in the lateral direction (near $\theta = 90°$) can be computed using the following formula :

$$\text{Width} = \frac{2\lambda}{Nd} \tag{4.13}$$

with N the number of antennas in the array and d the distance separating them. However, as the beam moves sideways (towards $\theta = 0°$ or $\theta = 180°$), the beam width broadens.

The total angle possible to scan is defined by the antennas in the array; in our case, it is $\beta = 75.9°$. In order to scan it completely, we must change the phase shift α, to move the direction of the main beam of the array. Using information from Figure 4.7, we can compute the number of scans needed so as to scan the whole orbit vertically; The total angle we wish to scan divided by the main beam width will give the number of times we will need to change the phase shift so as to illuminate another part of the total angle.

4.2 MIMO Radar

To improve the spatial resolution, a type of radar which could be interesting to implement for debris detection is the MIMO radar.
MIMO stands for Multiple Inputs Multiple Outputs. The principle of the MIMO radar is to create a virtual array of antennas, in order to improve the spatial and Doppler resolution. By spacing either the transmitting or receiving antennas, the virtual array is created [22].
The number of antennas of the virtual array can be computed as a convolution. As an example, we have three emitting antennas closely distributed, spaced by d between them, defined as [1 1 1]. We also have an array of three receiving antenna, however they are spaced by 3d defined as [1 0 0 1 0 0 1]. The resulting virtual array of receiving antennas is the convolution of the two arrays, giving [1 1 1 1 1 1 1 1 1]. From only 6 antennas in total, we obtain the equivalent of 9 antennas in the receiving array.
However, the receiving antennas must be capable of recognizing which signal comes from which antenna for the MIMO array to work. In order to distinguish them, multiples techniques exist :

- The emitting antennas can emit one at a time. This of course limits the speed at which we can scan the area and is not the most efficient way.
- It is also possible to send signals that are orthogonal to each other, and the post-processing can distinguish which signal is from which antenna.
- Another way is to send different waveforms from each emitting antenna.

As explained in Section 4.1.3, adding more antennas in the array narrows the mainbeam and thus improve the cell resolution of the radar. However, in the case of a satellite-mounted radar, increasing the spacing between the antennas is more complicated; It would require a deployment mechanism for the antenna array, which would be more prone to mechanical issues than the simple array of collocated antennas.

An illustration of the possibilities is shown in Figure 4.8, representing the virtual array of both a 1TX-64RX array and a 8TX-8RX array. The results are the same, however the second array has only 16 antennas against 65 for the first one. The sensitivity may be higher with more elements, but the MIMO array remains an interesting option.

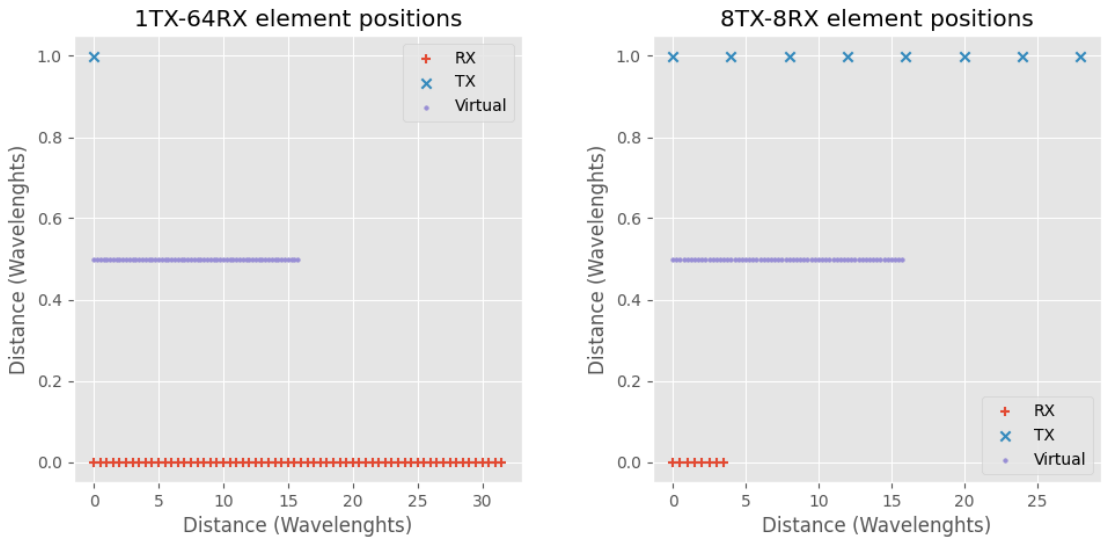

Figure 4.8: virtual array illustration. Image from [22]

CHAPTER 5

DEBRIS IN SPACE

Debris floating through space do not stay in the same "orientation"; they rotate on themselves, with a speed of rotation of the order of 1 Hertz. Since the radar is sending electromagnetic waves at a much higher rate, it is not a problem; we do not have to consider that the object is turning during a pulse. However, we shall account for all possible angles of view.

Debris in space come in various sizes and shapes. In order to correctly evaluate the power needed for the radar, an estimation of the debris' characteristics is needed.

5.1 Radar Cross Section

Radars do not simply see the surface of an object that is in front of them. There are multiple factors that will alter the response of the radar to the object. In order to still be able to compare the perceived surface of objects seen by a radar, we introduce the radar cross section. This quantity takes into account the fact that the power emitted by the radar antenna is distributed over a sphere whose radius is the distance between the radar and the object. The distribution is not uniform but depends on the gain of the antenna. It also considers that only part of the power emitted is reflected by the object, as the remainder is absorbed. Finally, this reflected portion is also spread non-uniformly across a sphere of the same radius as the previous one, and this influence is also factored into the radar cross section.

The radar cross section is obviously dependent on the surface of the target visible from the radar, but more importantly, on the wavelength relative to the size of the visible part of the target, as is shown in the figure 5.1. This graph represents the RCS response for a sphere, which has the same surface visible to the radar from any point of view.

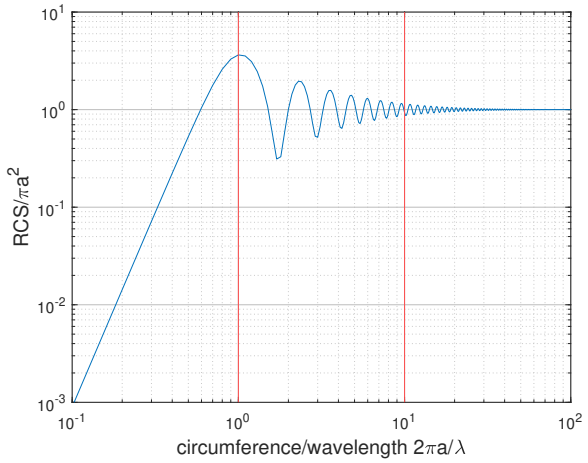

Figure 5.1: Radar cross section of a sphere of radius a compared to the wavelength; normalized with relation to the geometrical cross-section

The graph can be divided in three parts :

The Rayleigh region, where the wavelength is much larger than the radius of the target. The radar cross section is small in this region and thus the target is difficult to see.

The Resonance or Mie region, where we have interference between directly backscattered waves and waves creeping around the object. This creates the oscillating response in the figure.

The Optical region, where the wavelength is much smaller than the radius of the target. In this case, we find that the radar cross section tends toward the geometrical cross-section of the sphere.

But in space, the debris we are looking for will not be spheres, they will have many shapes difficult to predict. To begin with, we observe the case of a simple metallic cube, from all different directions. We simplify the problem by considering only the most exposed face of the cube to the radar wave. We use physical optics to approach this problem.

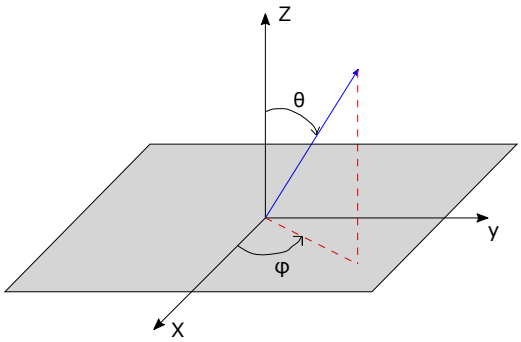

Figure 5.2: axis representation and reference to the plate debris. θ is defined from the z-axis, while ϕ is defined from the x-axis in the XY plane.

The radar cross section is defined from [23] as

$$\sigma = 4\pi R^2 \frac{|\mathbf{E_s}|^2}{|\mathbf{E_i}|^2} \tag{5.1}$$

where R is the distance between the radar and the target, $\mathbf{E_i}$ is the incident electric field at the level of the target and $\mathbf{E_s}$ is the scattering (returned) electric field at the level of the receiving antenna.
For our calculations, we make the hypothesis that the debris is made of a perfect conductor and we consider an incident electric field of a magnitude E_i. In the following, the physical optics (PO) approximation will be made. IT means that the involved surface current density $\mathbf{J}$ is the same as in the case of an infinite plate. This makes sens only when the plate size is of the same order or larger than the wavelength We obtain the following current density

$$\vec{J} = 2\hat{n} \times \vec{H}_{inc} \tag{5.2}$$

$$\vec{J} = 2\vec{H}_i e^{-jk(u_x^i x + u_y^i y)} \cos^p \theta \hat{e}_\perp \tag{5.3}$$

in which the term u^i, which is the direction vector of the incident electromagnetic wave, is divided in its x and y parts. $\hat{e}_\perp$ is an unit vector perpendicular to the normal vector to the plate.
In free space, we have the equality

$$E = \sqrt{\frac{\mu_0}{\epsilon_0}} H \Longleftrightarrow H_i = \frac{E_i}{\eta} \tag{5.4}$$

with $\eta = 377\Omega$ the free space impedance.
The scattered electric field can be computed in the following way :

$$\vec{E}_s = -jk\eta \frac{E_i}{\eta} \frac{e^{-jkR}}{4\pi R} \iint \vec{J} \cos^{1-p} \theta \, e^{jk\rho \cdot \hat{u}} dS \tag{5.5}$$

with k the wavelength number and ρ a vector to a point of the plate.
The cosine factors and their exponent come from the polarisation of the incident wave. In the case of a transverse magnetic polarisation (p=0), the incident magnetic wave is perpendicular to the normal of the plate, and the cosine factor does not appear at equation 5.2 or 5.3. However, in the computation of the scattered electric field (eq. 5.5), in order to calculate the part of the current density vector perpendicular to the direction of propagation, we must multiply it by $\cos\theta$. In the opposite case, with a transverse electric field (p=1), the magnetic field $\mathbf{H}$ is not perpendicular to the normal of the plate, and thus the cosine factor appears in equation 5.3, but then the obtained current density $\mathbf{J}$ is already perpendicular to the direction of propagation.
The radiation integral can be separated into two independent parts, in the x and y axes.

$$\vec{E}_s = -2jkE_i \frac{e^{-jkR}}{4\pi R} \cos\theta \, \hat{e}_\perp \iint e^{-jk(u_x^i x + u_y^i y)} e^{jk(u_x^s x + u_y^s y)} dS \tag{5.6}$$

$$= -2jkE_i \frac{e^{-jkR}}{4\pi R} \cos\theta \, \hat{e}_\perp \int e^{jk(u_x^s - u_x^i)x} dx \int e^{jk(u_y^s - u_y^i)y} dy \tag{5.7}$$

Since our radar is monostatic, that is the receiving antenna is at the same spot as the transmitting antenna, the incident and scattering vectors are the same except that they have opposite directions.

$$\begin{aligned}
\hat{u}_i &= (\sin\theta\cos\phi, \sin\theta\sin\phi) \\
\hat{u}_s &= (\sin(\pi-\theta)\cos(\phi+\pi), \sin(\pi-\theta)\sin(\phi+\pi)) \\
&= (-\sin\theta\cos\phi, -\sin\theta\sin\phi) \\
&= -\hat{u}_i
\end{aligned}$$

We can now integrate over the square plate which has a side length of L.

$$\vec{E}_s = -2jkE_i \frac{e^{-jkR}}{4\pi R} \cos\theta \hat{e}_\perp \int_{-L/2}^{L/2} e^{-jk2u_x^i x} dx \int_{-L/2}^{L/2} e^{-jk2u_y^i y} dy \tag{5.8}$$

$$\vec{E}_s = -2jkE_i \frac{e^{-jkR}}{4\pi R} \cos\theta \hat{e}_\perp \left[\frac{e^{-jk2u_x^i x}}{-jk2u_x^i}\right]_{-L/2}^{L/2} \left[\frac{e^{-jk2u_y^i y}}{-jk2u_y^i}\right]_{-L/2}^{L/2} \tag{5.9}$$

$$\vec{E}_s = -2jkE_i \frac{e^{-jkR}}{4\pi R} \cos\theta \hat{e}_\perp \frac{e^{jk2u_x^i \frac{L}{2}} - e^{-jk2u_x^i \frac{L}{2}}}{jk2u_x^i} \frac{e^{jk2u_y^i \frac{L}{2}} - e^{-jk2u_y^i \frac{L}{2}}}{jk2u_y^i} \tag{5.10}$$

we know that $\sin x = \dfrac{e^{ix} - e^{-ix}}{2j}$

$$\vec{E}_s = -2jkE_i \frac{e^{-jkR}}{4\pi R} \cos\theta \hat{e}_\perp L \frac{e^{jkLu_x^i} - e^{-jkLu_x^i}}{2jku_x^i L} L \frac{e^{jkLu_y^i} - e^{-jkLu_y^i}}{2jku_y^i L} \tag{5.11}$$

$$= -2jkE_i \frac{e^{-jkR}}{4\pi R} \cos\theta \hat{e}_\perp L^2 \frac{\sin(kLu_x^i)}{kLu_x^i} \frac{\sin(kLu_y^i)}{kLu_y^i} \tag{5.12}$$

We set $X = kLu_x^i$ and $Y = kLu_y^i$ and hence

$$\vec{E}_s = -2jkE_i \frac{e^{-jkR}}{4\pi R} \cos\theta \hat{e}_\perp L^2 \frac{\sin X}{X} \frac{\sin Y}{Y} \tag{5.13}$$

As we can see, the expression of the scattered electric field includes two sinc functions.

The radar cross section can be calculated

$$\sigma = 4\pi R^2 \frac{|-2jkE_i \frac{e^{-jkR}}{4\pi R} \cos\theta \hat{e}_\perp L^2 \frac{\sin X}{X} \frac{\sin Y}{Y}|^2}{|E_i|^2} \tag{5.14}$$

$$= 4\pi R^2 \frac{4k^2 E_i^2 L^4}{(4\pi)^2 R^2 E_i^2} \cos^2\theta \left|\frac{\sin X}{X} \frac{\sin Y}{Y}\right|^2 \tag{5.15}$$

$$= \frac{4k^2 L^4}{4\pi} \cos^2\theta \left|\frac{\sin X}{X} \frac{\sin Y}{Y}\right|^2 \tag{5.16}$$

$$= \frac{(2\pi)^2}{\lambda^2} \frac{4L^4}{4\pi} \cos^2\theta \left|\frac{\sin X}{X} \frac{\sin Y}{Y}\right|^2 \tag{5.17}$$

$$= \frac{4\pi L^4}{\lambda^2} \cos^2\theta \left|\frac{\sin X}{X} \frac{\sin Y}{Y}\right|^2 \tag{5.18}$$

As we can see, the radar cross section is dependent not on the distance, but on the wavelength and size of the target.

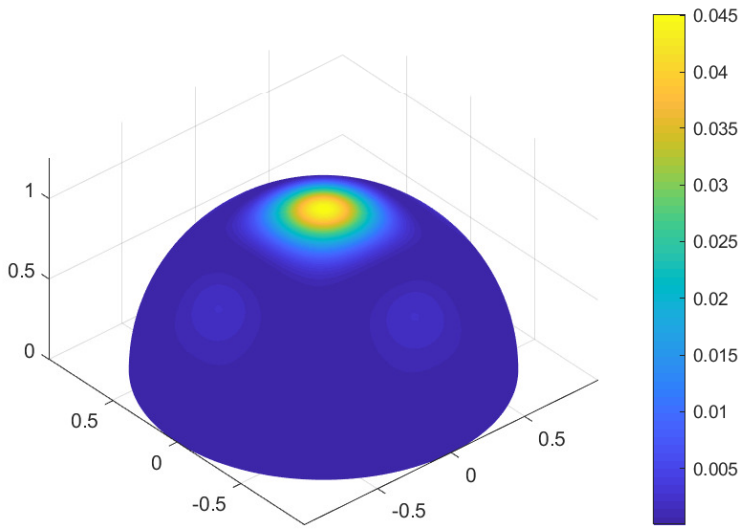

Figure 5.3: representation of the RCS on a sphere according to θ and ϕ.

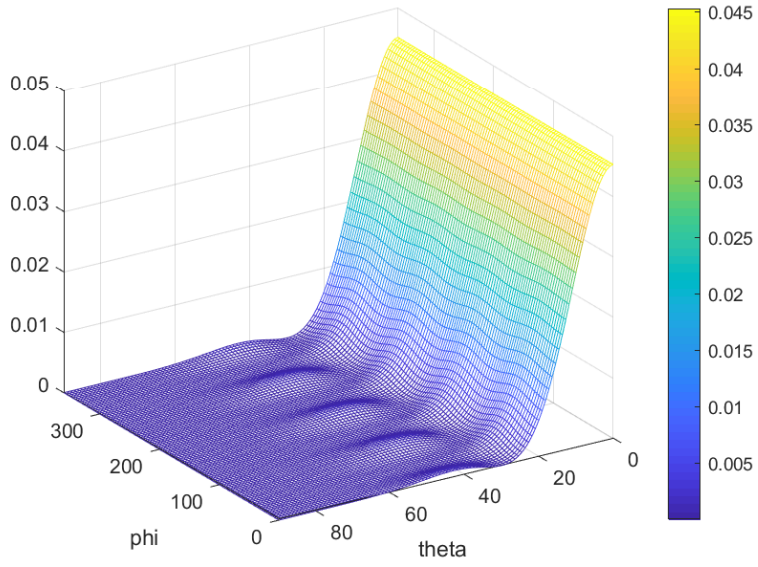

Figure 5.4: representation of the RCS according to θ and ϕ.

As we can see in figure 5.3, the RCS does not vary greatly as ϕ changes, but it depends much more with the angle θ. A sharp drop-off can be seen at around $\theta = 20°$. We notice that once the plate is no longer facing the radar, its radar cross section decreases significantly. For our plate with a side of 6 cm, the RCS seems to stay under 0.005 m^2 once θ is higher than 30°. This corresponds to approximately -23 dBm^2, which makes the plate very difficult to see for the radar. We notice slight variations in Figure 5.4 as ϕ varies for $30° < \theta < 60°$. This corresponds to the plate turning while staying in its own plane. The lower values appear when a corner of the plate is toward the radar. However this has very little effect for small θ, as stated earlier.

To compare with a sphere of the same surface, we could suppose that the radar cross section of a cube can be simplified to the face of the cube the most visible to the radar. This is determined by the angle θ relative to each face. To further simplify it, we suppose there is

always a face with an angle θ equal or lower than 45°. Thus to define the average RCS of a moving cube, we average the equation 5.18 with $\theta \leq 45°$. Of course this is very simplified compared to the reality, as there will be some times where none of the faces will have an angle smaller than that, while the interference (constructive or destructive) between multiple faces will not taken into account here.
We find the average is of 0.0131 m^2. This would compare to a sphere with cross sectional surface of the same value :

$$RCS_{sphere} = \pi R^2 = 0.0131 \text{ m}^2 \Leftrightarrow R = 0.0646 \text{ m} = 6.46 \text{ cm} \tag{5.19}$$

The cube would be roughly equivalent to a sphere with a radius of 6.46 cm. The cube's radar cross section is very similar to the one of a sphere having as a radius the side of the cube. Even though they have the same RCS, the sphere's geometrical cross section is larger (by a factor π) than the geometrical cross section of the cube.
Again, these results are for a target with a size the order of the wavelength of the radar.

5.1.1 Approximations

We can simplify the expression 5.18 by using a second order Taylor approximation for the sinc function :

$$\frac{\sin p}{p} \approx 1 - \frac{p^2}{6} \tag{5.20}$$

We know $X = kL \sin\theta \cos\phi$ and $Y = kL \sin\theta \sin\phi$, the product of the sinc functions becomes

$$= \frac{\sin\left(kL \sin\theta \cos\phi\right)}{kL \sin\theta \cos\phi} \frac{\sin\left(kL \sin\theta \sin\phi\right)}{kL \sin\theta \sin\phi} \tag{5.21}$$

$$\approx \left(1 - \frac{(kL \sin\theta \cos\phi)^2}{6}\right)\left(1 - \frac{(kL \sin\theta \sin\phi)^2}{6}\right) \tag{5.22}$$

$$\tag{5.23}$$

We believe the terms in $\cos^4\theta$ are negligible compared to the others, and we neglect them.

$$\left(1 - \frac{(kL \sin\theta \cos\phi)^2}{6}\right)\left(1 - \frac{(kL \sin\theta \sin\phi)^2}{6}\right) \approx 1 - \frac{1}{6}(kL)^2 \sin^2\theta \cos^2\phi - \frac{1}{6}(kL)^2 \sin^2\theta \sin^2\phi \tag{5.24}$$

$$= 1 - \frac{1}{6}(kL)^2 \sin^2\theta(\cos^2\phi + \sin^2\phi) \tag{5.25}$$

$$= 1 - \frac{1}{6}(kL)^2 \sin^2\theta \tag{5.26}$$

This result has the form of a Taylor approximation of a sinc function. We finally find

$$\frac{\sin X}{X}\frac{\sin Y}{Y} \approx \frac{\sin z}{z} \qquad \text{with } z = kL \sin\theta \tag{5.27}$$

We notice that once we simplify the equation, the dependency on ϕ disappears. This correlates with Figures 5.3 and 5.4, the change in the RCS is negligible as ϕ varies (but is much more dependent on θ).

We also wish to find an analytical expression of the radar cross section, and see if there is a constant that might approximate the relationship between the RCS and the actual area of the

plate.
Using the approximation from eq. 5.27, the RCS expression becomes

$$\sigma = \frac{(kL)^2 L^2}{\pi} \cos^2\theta \left| \frac{\sin(kL\sin\theta)}{kL\sin\theta} \right|^2 \tag{5.28}$$

We normalize the RCS by the area of the plate :

$$\frac{\sigma}{L^2} = \frac{(kL)^2}{\pi} \cos^2\theta \left| \frac{\sin(kL\sin\theta)}{kL\sin\theta} \right|^2 \tag{5.29}$$

To find the average of this normalized RCS, we integrate the equation (over a unit sphere since we are in polar coordinates).

$$\left(\frac{\sigma}{L^2}\right)_{avg} = \frac{3}{4\pi} \int_0^{2\pi} \int_0^{\pi/2} \frac{(kL)^2}{\pi} \cos^2\theta \left(\frac{\sin(kL\sin\theta)}{kL\sin\theta} \right)^2 \sin\theta d\theta d\phi \tag{5.30}$$

$$= \frac{3 \cdot 2\pi}{4\pi} \int_0^{\pi/2} \frac{(kL)^2}{\pi} \cos^2\theta \left(\frac{\sin(kL\sin\theta)}{kL\sin\theta} \right)^2 \sin\theta d\theta \tag{5.31}$$

$$= \frac{3}{2\pi}(kL)^2 \int_0^{\pi/2} \left(\frac{\sin(kL\sin\theta)}{kL\sin\theta} \right)^2 \cos^2\theta \sin\theta \, d\theta \tag{5.32}$$

There may be no analytical solution for the integral. A possibility is to approximate the squared sinc function by a Gaussian function, which has the same second order Taylor development :

$$\left(\frac{\sin x}{x}\right)^2 \approx e^{-x^2/3} \tag{5.33}$$

Compared to each other in Figure 5.5, we see that the approximation is good, at least for the lower values of θ. At higher values, the sidelobes of the sinc function are neglected.

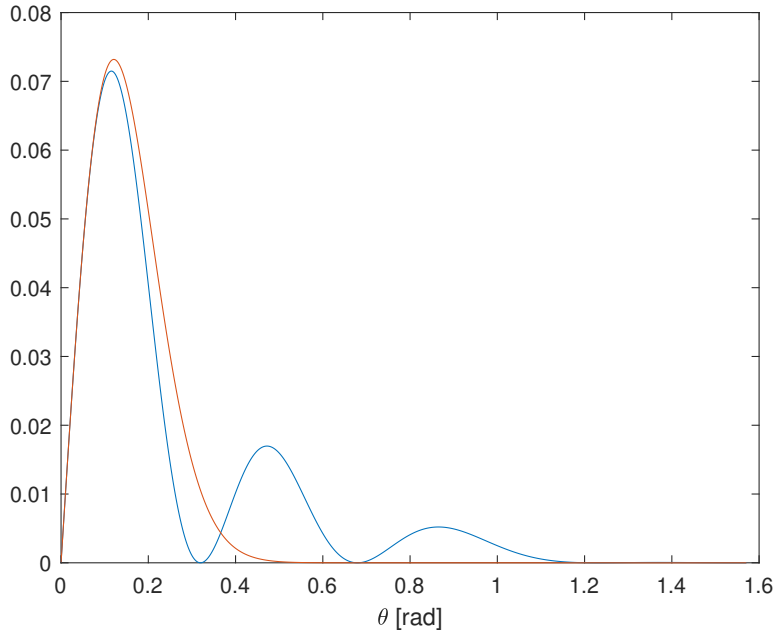

Figure 5.5: comparison between the integrands in equation 5.32 and the one obtained with the gaussian approximation (eq. 5.33)

The equation becomes

$$\left(\frac{\sigma}{L^2}\right)_{avg} = \frac{3}{2\pi}(kL)^2 \int_0^{\pi/2} e^{-(kL)^2 \sin^2(\theta)/3} \cos^2\theta \sin\theta \, d\theta \tag{5.34}$$

By neglecting the one of the cosine factors (supposing it does not have a too strong impact since the function is already low for larger θ), it becomes possible to integrate the equation analytically. We obtain

$$\left(\frac{\sigma}{L^2}\right)_{avg} = -\frac{3}{2\pi}(kL)^2 \int_0^{\pi/2} -\frac{(kL)^2}{3} e^{-(kL)^2 \sin^2(\theta)/3} \cos\theta \sin\theta \, d\theta \tag{5.35}$$

$$= \frac{-9}{2\pi}\left[e^{-\frac{(kL)^2}{3}\sin^2\theta}\right]_0^{\pi/2} \tag{5.36}$$

$$= \frac{-9}{2\pi}\left(e^{-(kL)^2/3} - 1\right) \tag{5.37}$$

From equation 5.37, we can see that when the frequency increase, so does the the wavenumber k. With a constant side length L, when the frequency tends toward infinity, the integral tends toward $\frac{9}{2\pi}$:

$$\lim_{f\to\infty}\left(\frac{\sigma}{L^2}\right)_{avg} = \frac{9}{2\pi} \tag{5.38}$$

For a plate of length $L = 2\lambda$, there is a difference of 0.1641 between the normalized RCS from equation (5.32) and the constant. It is thus relatively accurate for plates with a size the order of the wavelength.

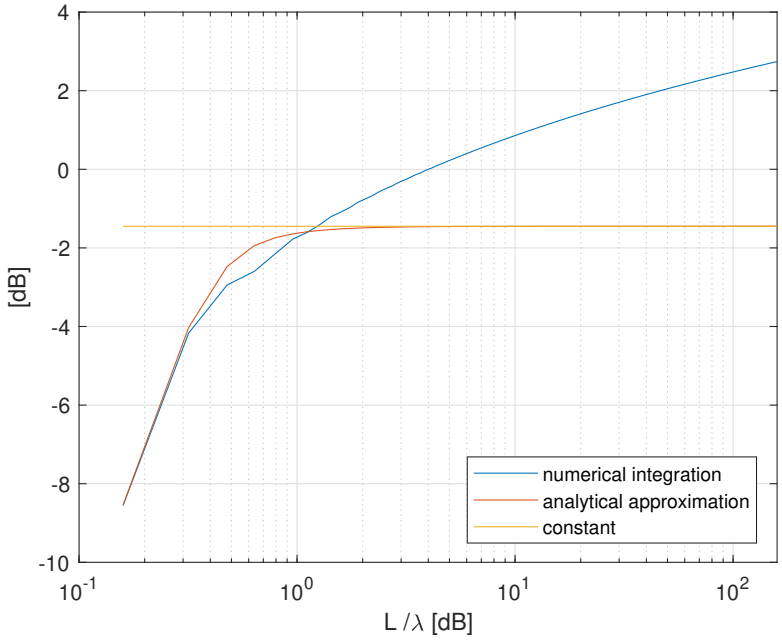

Figure 5.6: comparison between the numerical integration of the integral, the analytical solution with the Gaussian approximation and the constant obtained as frequency tends toward infinity.

As we can see in Figure 5.6, this constant is not accurate for wavelength much larger than the length L, and for much smaller wavelength as well.
For the smaller frequencies, the error becomes quite important and the constant is far from the correct value. However, at these frequencies, the analytical solution give results very similar to the numerical integration.

The difference between the constant and the real curve in the smaller frequencies is due to the fact that at lower values of kL, in equation (5.37), the exponent does not become small enough to be neglected.

As for wavelengths about a hundred time smaller than the length of the plate (therefore high frequencies), we have an error of 2.4 dB, and it continues to increase.
As can be seen in Figure 5.5 illustrating the integrands, this is due to the smaller lobes after the main one; as the frequency increases, the number of secondary lobes does too and they become more significant in the integration. However the increase is slow, and we reach a difference of 3 dB only at very high frequencies or very large targets in terms of wavelengths.
With some curve fitting, it is possible to find a function that follows the numerical integration in the logarithmic scale when the frequency gets higher. The expression of this curve is the following :

$$f\left(\frac{L}{\lambda}\right) = 10\log_{10}\left(\frac{9}{4\pi}\right) + 2\log_{10}\left(\frac{L}{\lambda}\right) \tag{5.39}$$

This curve is plotted in purple in Figure 5.7.

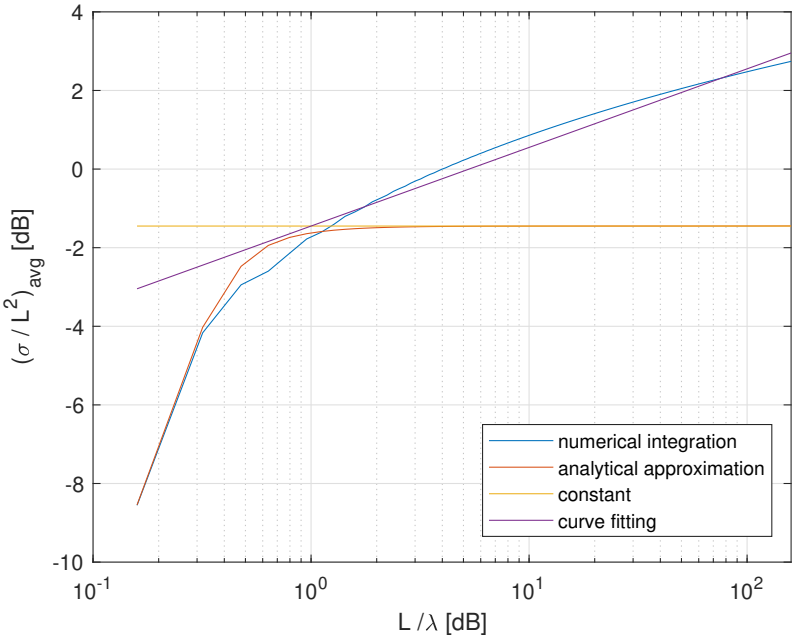

Figure 5.7: The purple curve is the function made to fit the numerical integration at higher frequencies

The constant, analytical solution and curve fitting allow one to roughly estimate what the average RCS over the physical area of the plate would be. It is useful as a first approximation, for a fast calculation without the need to integrate the more complete but complex expression of the RCS.

5.1.2 Dependency on the frequency

As stated earlier, the radar cross section is dependent on the wavelength used by the radar, inversely proportionally to the squared wavelength. However, as the frequency increases, it becomes more important to be facing the plate in order to see the highest RCS values.
In Figures 5.8a and 5.8b, we can observe the RCS response depending on the orientation of the plane relative to the radar with different frequencies, 2.4 GHz and 10 GHz. The maximum

RCS surely increases with the frequency, but we can see that the higher value of RCS are only attained as the plate is well aligned with the radar, which does not happen more often than the other orientations of the plate. Therefore, even if it might seem more attractive to use a higher frequency in order to have a better RCS, the plate might actually be harder to see at different angles. The increase in frequency thus might decrease our chances to detect the object.
It is another compromise that should be carefully analysed when choosing the frequency at which we work at.

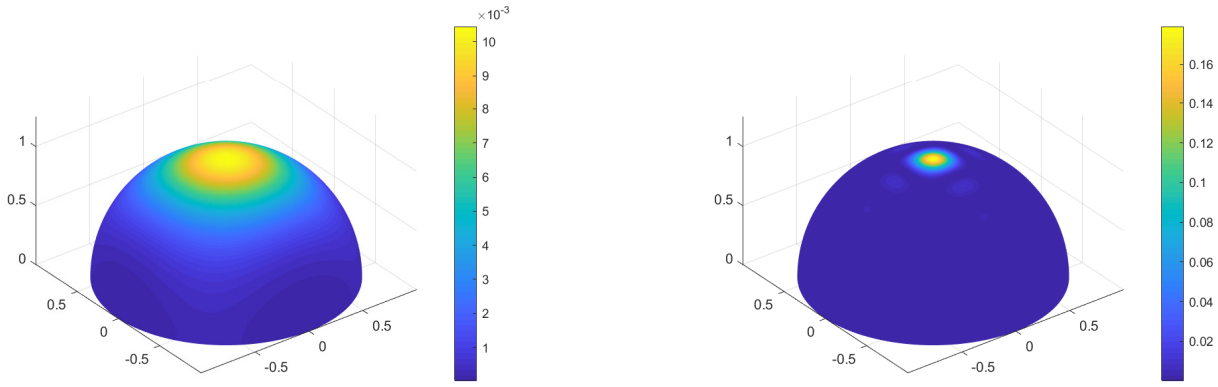

(a) RCS at 2.4 GHz

(b) RCS at 10 GHz

Figure 5.8: RCS response for a square plate with a side length of 6 cm. We can see that, even though the response is lower, the RCS at 2.4 GHz does not need the radar to face the plate as accurately as at 10 GHz.

The RCS dependence on the orientation is also quite dependent on the size of the plate. As the plate grows larger, the maximum RCS increases, but the response when the plate is not facing well the radar diminishes.
This is due to the sinc function depending on the length of the square : equation 5.18 shows the sinc functions depends on X or Y, which are defined as $kLu^i_{x/y}$. As L increases, the total RCS responses increases with L^2, but the sinc functions get narrower. A comparison between two such sinc functions with different argument illustrates this in figure 5.9. This also needs to be taken into consideration for the choice of the operating frequency.

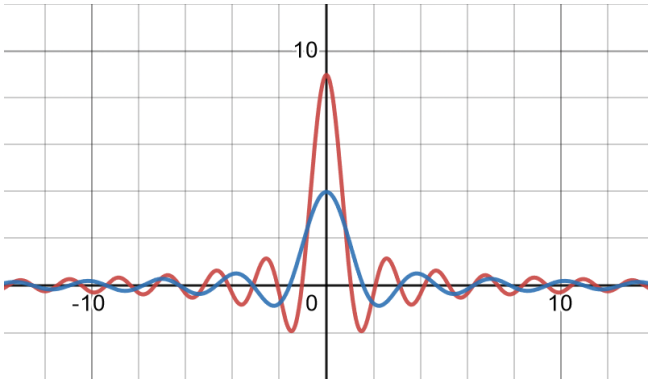

Figure 5.9: comparison between two sinc function. The red curve is the function $9\frac{\sin(3x)}{3x}$ and the blue curve is $4\frac{\sin(2x)}{2x}$. While a larger plate would get an increase from the L^2 term, the amplitude distribution would be more concentrated around the normal to the plate.

In Figure 5.10, we can see the response of the plate (keeping the same size of 6 cm) past the main beam at different frequencies. The values are relatively close, about the same order of magnitude. However, the main beam of the higher frequencies are much stronger. Therefore, if the radar is calibrated to detect the high values when the plate is well aligned with the radar, it will have a much harder time detecting at other angles when using higher frequencies than lower ones.

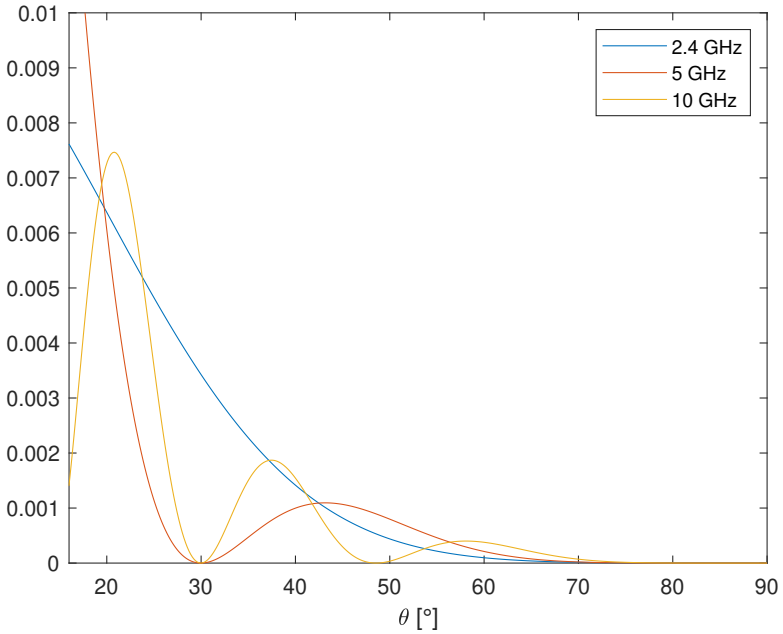

Figure 5.10: RCS response of a 6x6 cm plate past the main beam, at different frequencies

Another illustration of this case is provided by the histogram of the RCS. In Figure 5.11, histograms have been given on the RCS at 4 different frequencies : 1, 2.4, 5 and 10 GHz. In all four cases, the majority of angles have an RCS in the lowest brackets of values. However, as the frequency rises, the phenomenon only increases; the distribution becomes more uneven and the high values of RCS (in the right of the graphs) are getting rarer.

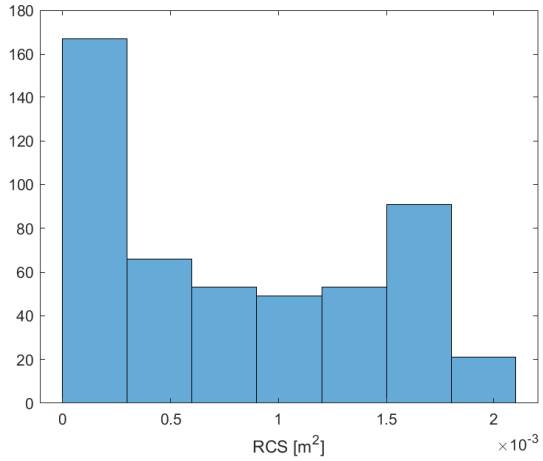

1 GHz

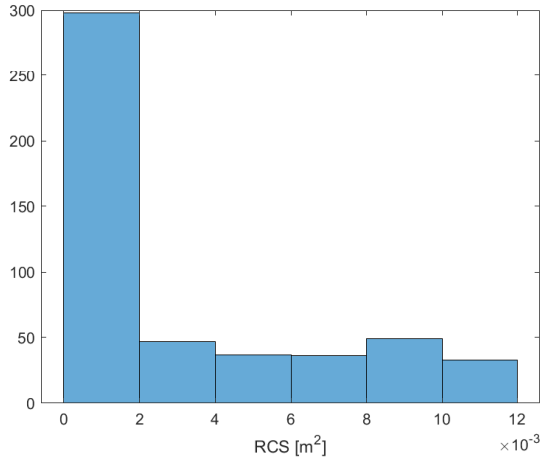

2.4 GHz

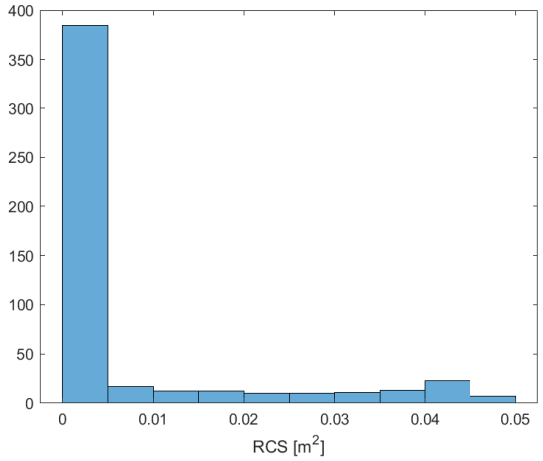

5 GHz

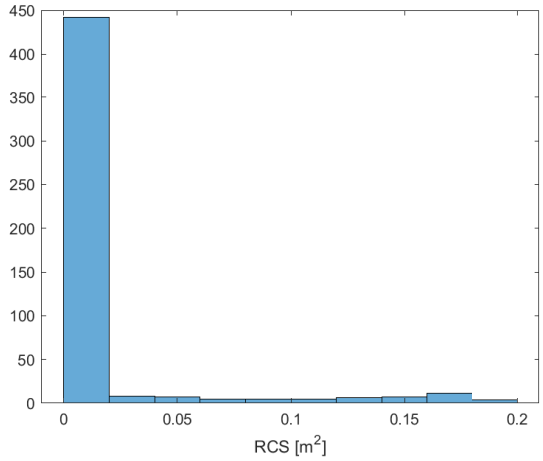

10 GHz

Figure 5.11: Histograms at different frequencies

A comparison of the average response for the cube of side length of 6 cm at different frequencies has been done. The average RCS slowly increases with the frequency as expected,

5.1.3 Validation of the physical optics

To verify the validity of physical optics used here to compute the RCS response of the plate, its results were compared with results obtained using the method of moments, known for being extremely precise for the calculation of radar cross section.

Jean Cavillot kindly provided a comparison between these results at a frequency of 20 GHz, for a plate with a side length varying from an eighth to four times the wavelength.

f = 20 GHz	4 λ	2 λ	3/2 λ	λ	3/4 λ	$\lambda/2$	$\lambda/4$	$\lambda/5$	$\lambda/8$
$\lvert E_s\rvert/\sqrt{k_0\eta_0}$ (PO - 1)	18.860	7.663	2.888	1.120	0.7663	0.484	0.087	0.038	0.007
$2\ \eta * S$ (MoM - 2)	19.111	7.465	2.69	1.194	0.6719	0.298	0.074	0.047	0.018
(1)/(2)	0.986	1.026	1.074	0.938	1.1405	1.623	1.170	0.796	0.397

Table 5.1: comparison between the scattered electric field on square plates at 20 GHz from Physical Optics (PO) and Method of Moments (MoM).

On the fourth line in Table 5.1, the ratio between scattered electric fields (the ratio of the RCS would just be the square of these) from the optical physics and the method of moments is quite close to 1 for the larger plates, down to the side length of $\lambda/4$. This validates the physical optics solution, as they are very similar to the results of the method of moments, apart from the plate the size of half a wavelength where the physical optics response is stronger. This might be due to a resonance effect, where the plate acts as a resonating dipole.
The two methods' results start to diverge when the size of the plate drops below a quarter of the wavelength, showing that the physicals optics are not accurate when the size of the square debris decreases a lot compared to the wavelength of the radar.

While our results for plates the size of a wavelength and greater are quite accurate, they seem to be much lower for the plate smaller than a quarter of a wavelength. Physical optics do not seem to be accurate for these smaller plates and we should avoid using this technique to compute the RCS of small (compared to the wavelength) targets.

CHAPTER 6

ANTENNA DESIGN

For the radar to correctly scan the geostationary orbit and detect the smaller debris and their position, the antenna needs to be designed with a particular objective in mind : the vertical cell resolution is defined by the width of the main beam of the antenna. A small cell resolution is needed to have an accurate measurement of the position of the debris; we thus need to design the antenna to be as directive as possible.

In the first draft the dimensions of the antenna were set to be around one meter by one meter, which seems to be an appropriate choice for our satellite, allowing us to have many elements for our array while keeping a decent size for a satellite.

Since the radar operates at a frequency of 5 GHz, a single microstrip antenna patch square size would default to half a wavelength, 3 cm or a bit less with the use of a high-permittivity dielectric material. A spacing of half the free-space wavelength is usually introduced between the patches, in either X and Y directions. This makes an antenna array of 16 times 16 series-fed patch antennas. This first draft of what the antenna could look like is illustrated in Figure 6.1

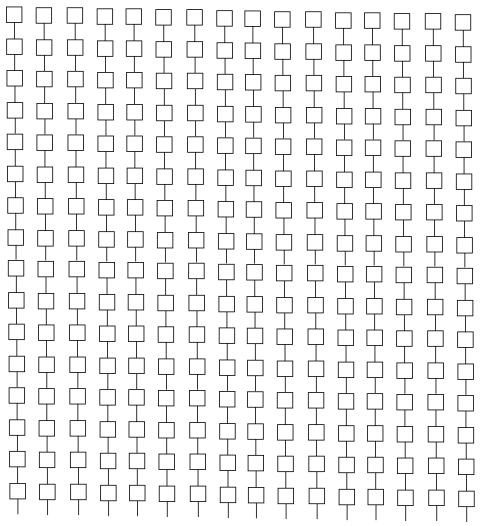

Figure 6.1: basic antenna array design with series-fed patches.

6.1 Parameters of an antenna

In the design of an antenna, multiple parameters result from the geometry chosen. The prevalent ones are the following.

6.1.1 Directivity

The antenna's main lobe magnitude and direction will change with the design. The magnitude, expressed in dBi (decibels relative to isotropic, that is the same radiation in every direction), is especially important as it will greatly influence the capability of the radar to distinguish between targets.

6.1.2 S-parameter

The S-parameter represents the relationship between the input and output at two ports. A port has an S-parameter with itself, corresponding to the power that is reflected back to the port, also known as the reflection coefficient or return loss, expressed in dB. If the reflection coefficient is equal to 0 dB, no fraction of the power is sent for to the antenna, all of it is going back to the generator. Obviously we need to have this reflection coefficient as low as possible.

6.1.3 Side Lobe Level

The side lobe level (SLL) represents the difference between the magnitudes of the main lobe and the lobes around this main lobe. In order to have a greater cell resolution, we try to have a low SSL.

The physical design of a patch antenna consists of three layers (see Figure 6.2). The first one is the ground plane, made of copper and on the bottom of the antenna. The second layer is the dielectric substrate. The one we chose is the FR-4 epoxy for its popularity and its low cost. It has a permittivity of $\epsilon_r = 4.3$ and the layer is 1.5 mm thick. The third layer is the patch that will conduct the current, again in annealed copper. Both ground and patch layers are 0.035 mm, thin compared to the substrate. In a later stage of this study, FR-4 should be replaced by a material with lower losses and should be better qualified for space applications.

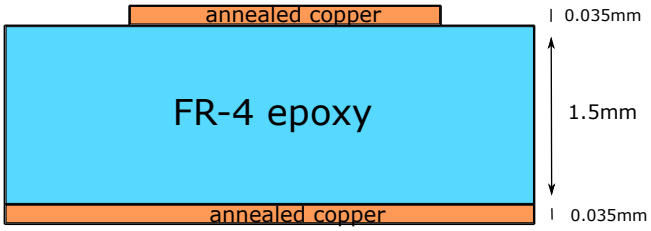

Figure 6.2: sideview of a patch antenna.

All simulations were carried out using the CST (Computer Simulation Technology) commercial software from Dassault Systemes.
A first antenna was created using the length and width of patches calculated using formulas from *Antenna theory - Analysis and design* by C. A. Balanis [24]. A slighty modified equation for the length found online from *Pasternack* [25] yielded better results, and is used instead.

$$Width = \frac{c}{2f_0\sqrt{\frac{\epsilon_r+1}{2}}} \tag{6.1}$$

$$\epsilon_{eff} = \frac{\epsilon_r + 1}{2} + \frac{\epsilon_r - 1}{2}\left(\frac{1}{\sqrt{1 + 12(h/W)}}\right) \tag{6.2}$$

$$Length = \frac{c}{2f_0\sqrt{\epsilon_{eff}}} - 0.824h\left(\frac{(\epsilon_{eff} + 0.3)(W/h + 0.264)}{(\epsilon_{eff} + 0.258)(W/h + 0.8)}\right) \tag{6.3}$$

We find W = 18.4 mm, $\epsilon_{eff} = 3.8234$ and L = 13.96 mm.
In a first instance, all the patches have these same dimensions, and the feedlines are such that consecutive patches radiate in phase. The width of the feedlines is computed using the CST integrated calculator in order to reach 50Ω at the port to match the input impedance.
The results of this simple design are already pleasant :

- the gain in the main beamwidth reaches 17.3 dBi, a good start for a single antenna.
- the S-parameter reaches -8 dB, which could be improved a little.
- the sidelobes are 10.7 dB lower than the main lobe, there is significant room for improvement here.
- the half power beamwidth is of 7° in a $\phi = 90°$ cut where ϕ is defined from the X-axis toward the Y-axis in Figure 6.3. In the perpendicular cut ($\phi = 0°$), the beamwidth is 75.9°.

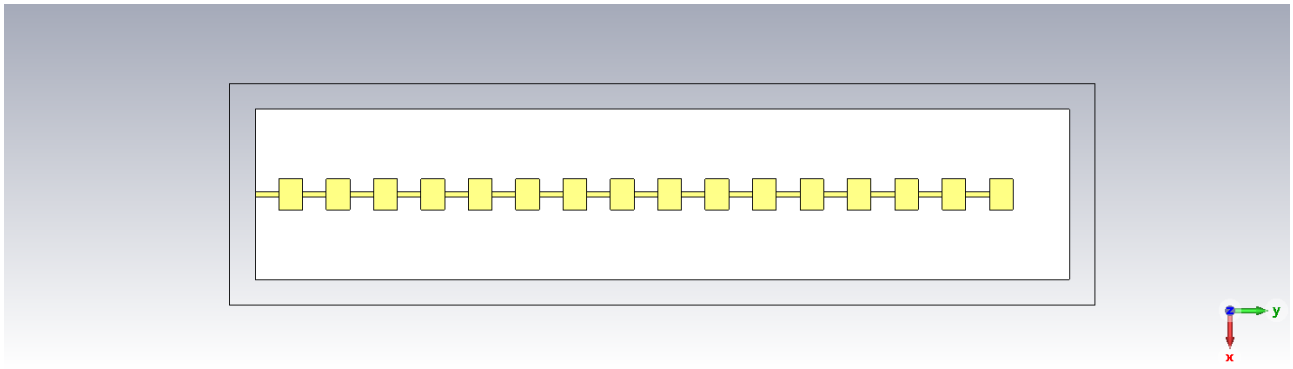

Figure 6.3: Design of the antenna. All the patches have the same dimension.

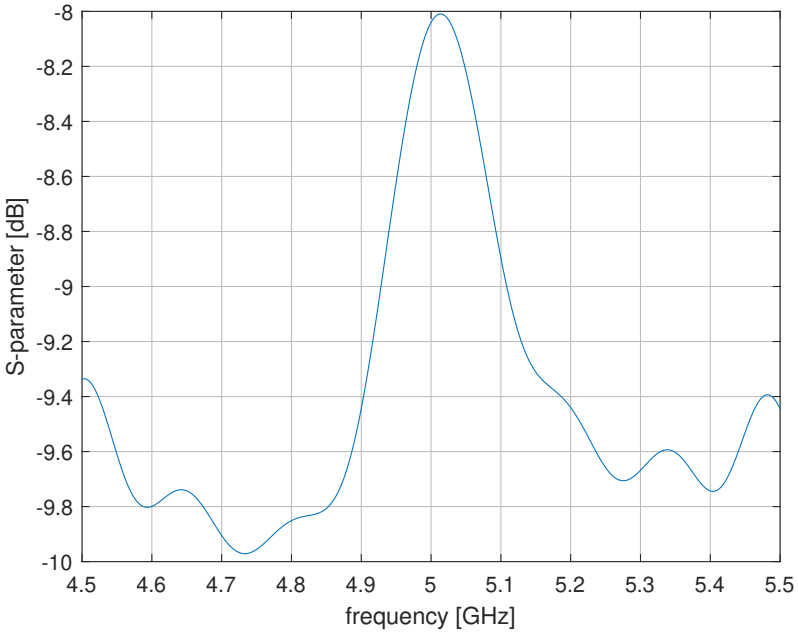

Figure 6.4: S-parameter of the antenna versus frequency.

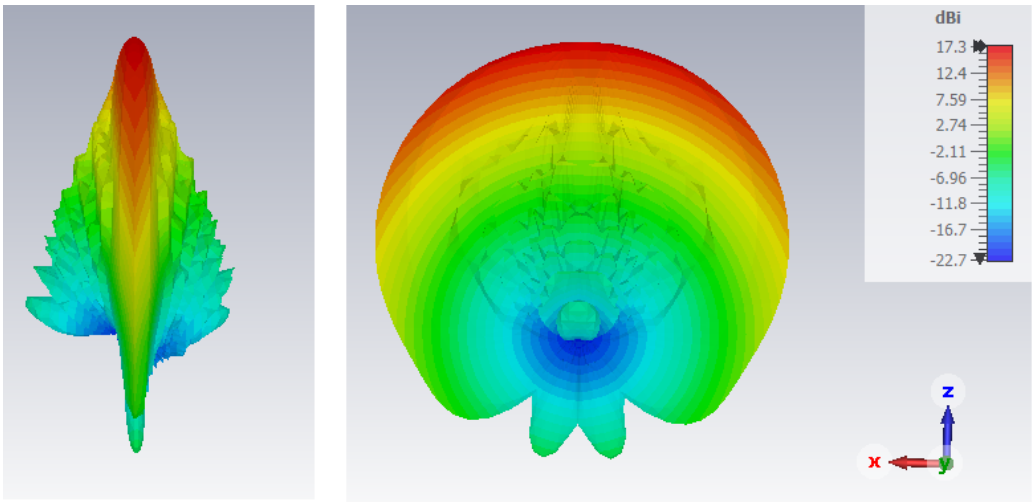

Figure 6.5: Far field of the antenna. The left image is a view in a $\phi = 90°$ cut while the right image is in a $\phi = 0°$ cut plane.

6.2 Reducing the sidelobes

A possibility for improvement of the sidelobes is to change the length of the 16 patches according to a squared cosine distribution. This would reduce the sidelobes level at the cost of diminishing a bit the gain in the half power beamwidth. This will also have an influence on the S-parameter. However we do not want the patches the furthest from the center to be too small, otherwise it will lower the gain too strongly. As a rule, I did not use values lower than a third of the initial width of the patches.

The technique used to choose the widths for each patch is to sample the squared cosine with a number of equidistant points between $-\pi/2$ and $\pi/2$. The 16 center points are then used as multiplying factors for the width of the patch. The squared cosine is a symmetrical

function around 0, so we only have 8 different factors. The values are shown in Table 6.1, and the distribution is illustrated in figure 6.6.

patch	1, 16	2, 15	3, 14	4, 13	5, 12	6, 11	7, 10	8, 9
factor	0.9966	0.9698	0.9177	0.8431	0.75	0.6434	0.5291	0.4132

Table 6.1: multiplying factor depending on the position of the patch in the antenna

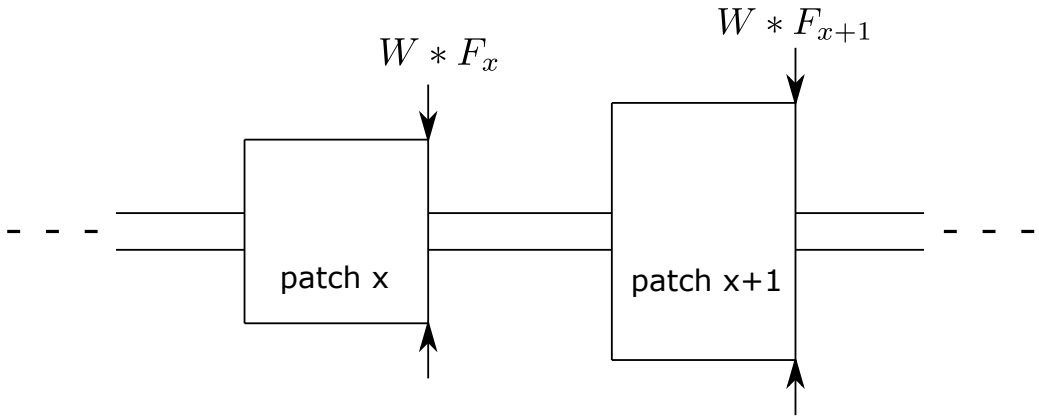

Figure 6.6: Width modification using the squared cosine factors

This width distribution resulted in the following antenna :

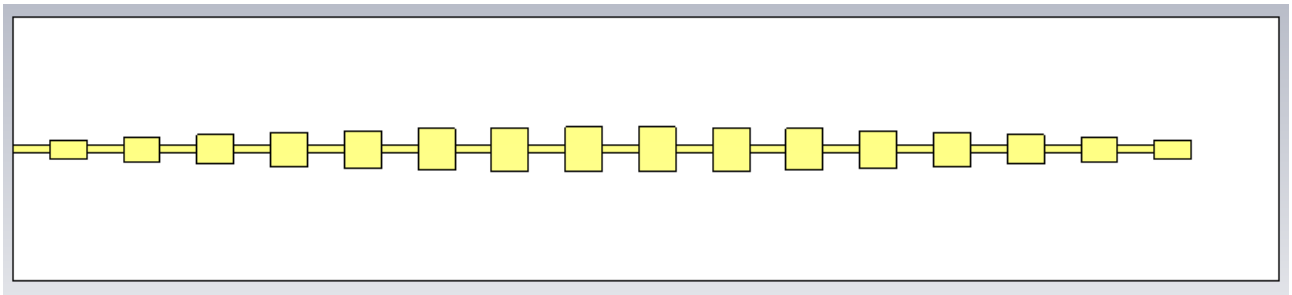

Figure 6.7: Design of the antenna with cosine distribution

With this approach, we may imagine the last few patches to be under illuminated since a lot of power already leaks out at the first few patches. In retrospect, it might have been interesting to increase the size of the last few elements to increase their illumination.

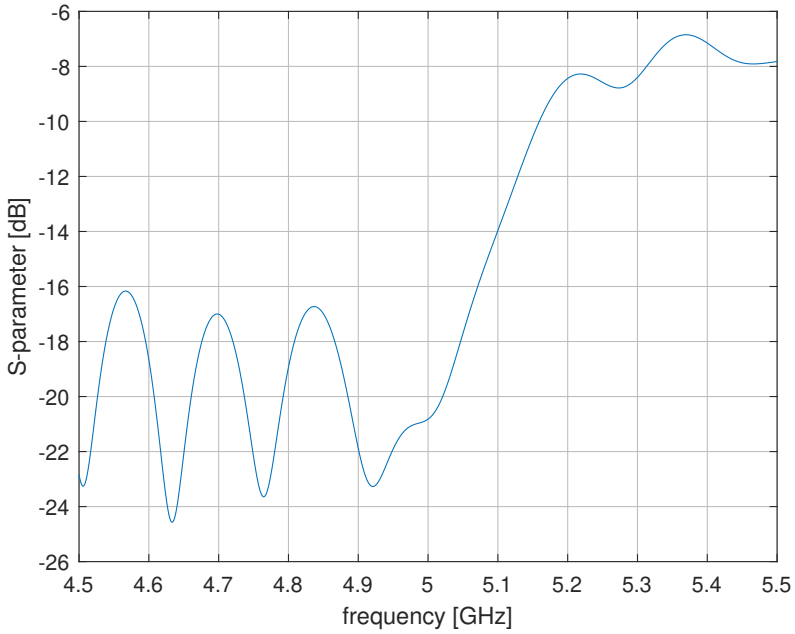

Figure 6.8: S-parameter of the cosine distribution antenna.

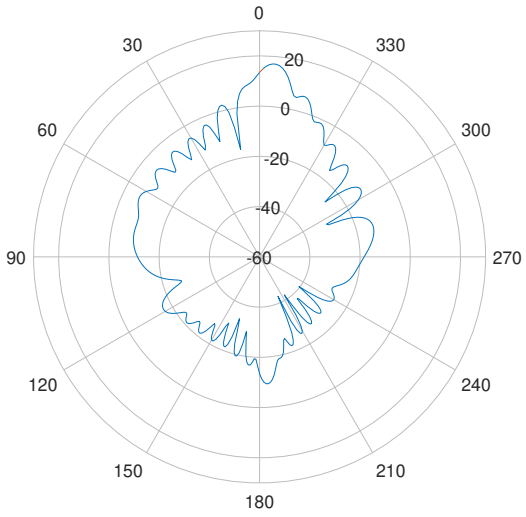

Figure 6.9: $\phi = 90°$ cut of the far field of the cosine distributed antenna. It reaches 17 dB in the main beam. The main beam is slighty tilted by 4.5°. In the $\phi = 0°$ cut, the far field does not change noticeably compared to the previous antenna, with a half power beamwidth still of 75.9°

Unfortunately, this technique did not prove to decrease the SLL significantly (only 0.1 dB) for the antenna of 16 patches. However, it did improve nicely the S-parameter, the bandwidth (10 MHz around 5 GHz) being below -10 dB, a nice improvement compared to the simpler antenna, but it also decreased slightly the main lobe magnitude from 17.3 to 17 dBi.

Since the S-parameter of the first antenna was a bit too high for our application, the second antenna is taken. The slight improvement on the sidelobes level and the much lower reflection coefficient makes the trade-off with the decrease of 0.3 dB for the gain worthwhile.

6.3 Array of antennas

Once the design of a single antenna is completed and the results are satisfying, the array of antenna can be designed.

The gain of the array should be approximately the multiplication of the single antenna times the number of antennas we set in parallel. Thus we should improve the gain by a factor $10\ log_{10}(N)$ with N being the number of antennas in the array. The first objective was to set 16 antennas in the array, for an increase of the gain by 12 dB. This would bring the gain up to 29 dBi, close to the 30 dBi we were aiming for.

The CST software allows the analysis of an array to be done directly from a single antenna, specifying the number of antennas in the array and the distance between adjacent antennas. After testing multiple values for the spacing between the antennas to maximise the gain, with an array of 16 antennas separated by 56 mm, we observe a directivity of 30.7 dB with the antennas without the cosine distribution of the width, i.e. above the 30 dB we were aiming for.

However, this spacing will not allow for a too large phase shift in the array in order to scan the orbit before introducing grating lobes. This makes another trade-off to consider : increasing (up to approximately) the spacing between the antennas in the array will improve the gain but will add grating lobes faster as we change the phase shift, thus limiting the area we can scan, as mentioned in Section 4.1.3. This limit is defined in the following section.

6.4 Final choice of the antenna array

The choice made for the antenna to use for the radar is set to the squared cosine distribution antenna. Its improvement on the S-parameter, as well as the slight amelioration of the sidelobes level make up for the slight decrease of the gain.
Multiple spacings have been considered : 3, 4, 5, and 5.6 cm with a main beam gain of 27.8, 29, 29.9 and 30.3 dB respectively. While the 3 cm spacing allows to scan the total possible angle, limited by the single antenna design, the total gain is not favorable to detect debris.
Again, the 4 and 5 cm spacing allows scanning the whole zone without grating lobes and the increase in gain is nice.
However, we observe that with a spacing of 5.6 cm, the gain is at 30.3 dB, with an angle of 7° at the bottom and top that we cannot scan without the appearance of grating lobes. This means the total scan angle is reduced to 68.9°, a very reasonable angle considering the increase in gain in exchange.

Additionally, as explained in Section 4.1.3, the increase of spacing between the antenna also narrows the main beam width, thus improving the cell resolution of the radar in the vertical direction.

Eventually, the choice of the antenna array converges towards the spacing of 5.6 cm, allowing a greater gain and cell resolution, at the small cost of a 14° smaller area of scan. It seems this choice will grant the radar an improvement in both precision of the position of the target, as well as an enhanced detection of smaller targets thanks to the increase in gain.

The parameters of this array are the following :

- Maximum gain of 30.3 dB
- Half power beamwidth of 7.8° in the plane $\phi = 90°$ at an angle of $\theta = 4.5°$.
- The beamwidth in the plane $\phi = 0°$ varies from 7.7° to 8.5° and its moves from $-24.7°$ to 24.7° thanks to the phase shift
- S-parameter of approximately -20 dB around 5 GHz.
- Sidelobes level of -10.8 dB

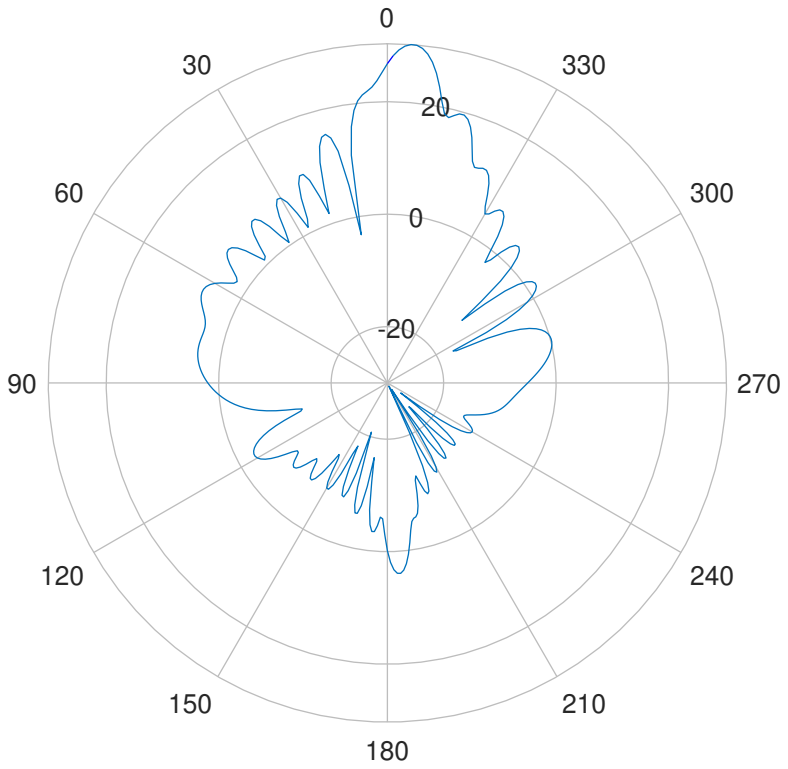

Figure 6.10: $\phi = 90°$ cut polar plot of the far field of the array of 16 antennas, with no squared cosine width distribution. The main beam, at $\theta = 0°$, reaches above 30 dB. The antennas have been analyzed at the same time to include the effects of mutual coupling.

The dimension of a single antenna is of 447 mm × 17 mm, and the whole array is 447 mm × 896 mm, not counting the additional area of dielectric around the patches (of the order of 40 mm on each side). It is about half of the initially targeted square meter; it seems reasonable for an antenna devoted to mounting on a satellite.

Referring back to the vertical scan in section 4.1.3, we find that since the largest beam to scan vertically is 8.5° wide and the narrowest is 7.7°, to scan the whole angle of 61.9°, we would need to move the beam 6 or 7 seven times. The situation is illustrated in Figure 6.11.

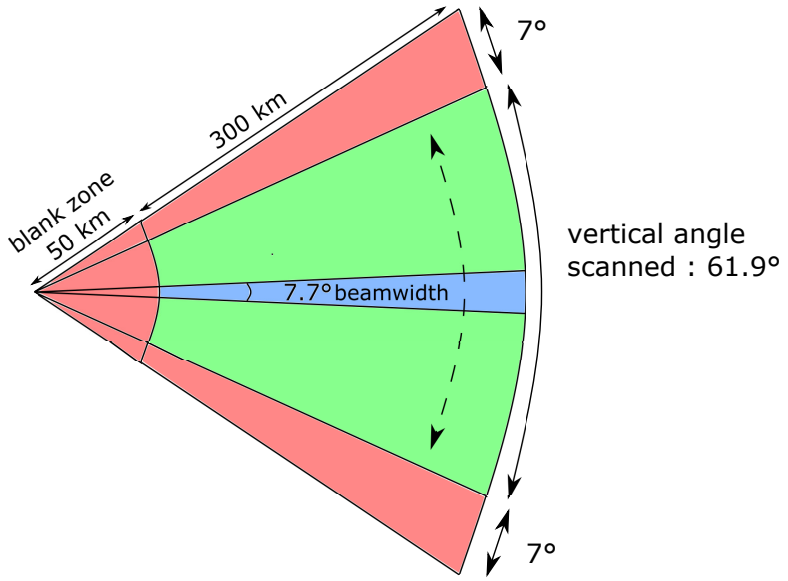

Figure 6.11: Illustration of the angle scanned. With phase shifts, the blue beamwidth can move up and down to scan the whole green zone. The red zones cannot be scanned, either because of the blank zone or because of the appearance of grating lobes.

CHAPTER 7

RADAR RANGE EQUATION

The ability of the radar to detect the reflected wave from an object depends on many parameters. The radar range equation gives us the signal-to-noise ratio of that echo considering these parameters :

$$\text{SNR} = \frac{P_t G^2 \lambda^2 \sigma}{(4\pi)^3 R^4 k T_s B_n L} \tag{7.1}$$

where the parameters are the following :

- P_t the transmitted power
- G the gain of the transmitting and receiving antenna
- λ the wavelength of the radar
- σ the radar cross section of the object
- R the distance between the radar and the object
- k Boltzmann's constant
- T_s the system noise temperature
- B_n the signal bandwidth
- L the total system losses

The product kT_sB_n is the average noise power and the term $\frac{\lambda^2}{(4\pi)^3 R^4}$ represents the propagation losses.
The system losses are usually around 7 dB. This factor represents the losses in the transmission lines and in the connections, as well as from any components that might be between the transmitter and the antenna. Part of it is also the noise factor coming from the electronics intrinsically, valued at 4 dB.
As was said earlier, the power transmitted to the radar P_t will depend on the solar panels surface limitations, as well as on the length of the pulses. The gain of the antenna depends on their design. In our case, we consider the receiving and emitting antenna to have the same gain.
The distance between the object and the radar has a strong influence on the SNR. Our objective is for an object at a distance of around 150 km to be perceptible, maybe even up to 200 km.
The radar cross section σ, which varies with the size and shape among other things, is detailed in Chapter 5.

The signal-to-noise ratio can be expressed in a different way. The previous one assumes the gain of the antenna is constant, but it is possible to make another assumption : a constant effective aperture.
The effective aperture is defined as the area receiving an amount of power from the reflected wave. It can be related to the gain in the following way :

$$A_e = \frac{\lambda^2}{4\pi} G \tag{7.2}$$

where G is the antenna gain. the latter can be replaced in equation 7.1 by its expression in terms of A_e and the SNR becomes

$$\text{SNR} = \frac{P_t A_e^2 \sigma}{4\pi R^4 \lambda^2 k T_s B_n L} \tag{7.3}$$

The wavelength moves from the numerator to the denominator and it is now beneficial to work at higher frequencies.
For aperture-type antennas, the effective aperture in our case is approximated as the area of the patch antenna array times a 70% aperture efficiency. It also depends on the angle of attack between the antenna and the debris; if the debris is at an angle θ from the normal to the antenna, then a $\cos\theta$ factor is added. The effective aperture is thus defined as

$$A_e = \text{Area} \cdot 0.7 \cdot \cos\theta \tag{7.4}$$

Where we have $|\theta| \leq 31°$, the maximum angle at which we can send and thus receive signals. The area of the array is about 0.5 m^2. This results in an effective aperture varying between 0.3 and 0.35 m^2.

The SNR resulting from each formula do not differ too much in this case. The only parts of the SNR equation changing are the following :
With constant gain : $\frac{G^2\lambda^2}{(4\pi)^3 R^4} = -46.38$ dB
With constant effective aperture : $\frac{A_e^2}{4\pi R^4 \lambda^2} \, \epsilon \, [-45.22, -46.56]$ dB
The variation does not impact much the results at the frequency of 5 GHz and so the SNR with constant antenna gain will be used in our computations.

7.1 Choice of frequency

The frequency of the radar has an impact on multiple things, and must be carefully considered. Depending on the SNR formula used (either considering constant gain with eq. (7.1) or constant effective aperture with eq. (7.3), the frequency can improve or deteriorate the propagation losses.

The wavelength is also involved in the radar cross section. While a candid look at the equation of the RCS (eq. 5.18) might make you think the RCS will only improve as the frequency increases, it is more complex than that. As discussed in Section 5.1.2, for a flat debris such as a plate, while the maximum value of the RCS will indeed increase, it will also get concentrated around the normal to the plate, and will degrade much faster at other angles. The targets might become more visible when facing well the radar, but they will also be harder to detect at other angles of incidence.

Moreover, the frequency choice will affect the antenna dimension as well, of which the elements usually have a size of the order of half a wavelength. Increasing the frequency therefore

decreases the overall size of the antenna, and allows for a more compact design or to add more elements to the antenna while keeping the same area, thus improving the gain the SNR. Maintaining a given effective area while increasing the frequency will require an increase of the number of elements and hence of active channels. This will in turn increase the consumption as well as the complexity of the array.
Size can be a limiting factor especially for an application on a satellite.

Our choice has been set on 5 GHz, it seems the compromise between a good relatively high RCS and the reasonable distribution of the RCS around the normal of the plate is good. Working at this frequency should allow us to detect relatively small targets even if they are not facing the radar perfectly and have a reasonably sized antenna array.

7.2 Improving the SNR

To further improve the SNR, two methods are implemented : pulse compression and coherent integration.

7.2.1 Pulse compression

Pulse compression is used to improve the SNR and the distance resolution.

Without pulse compression, the duration of the pulse defines the depth resolution : if the pulse lasts for a time T, then a depth resolution cell will be $c\,T$. If two objects are not spaced by more than this resolution, their echo will be mixed and they will not be distinguishable.

But if we apply the cross-correlation between the emitted and received signals with linearly frequency-modulated pulses, we obtain a cardinal sine [26]. The power which was uniformly distributed in the simple pulse, is now concentrated in the main lobe of the sinc function. This main lobe has a width of $\frac{1}{B}$, where B is the bandwidth. With a smart choice of the pulse length and bandwidth, the echo is now much shorter and it is possible to differentiate two targets that are closer than the previous depth resolution, as can be seen in the following figures.

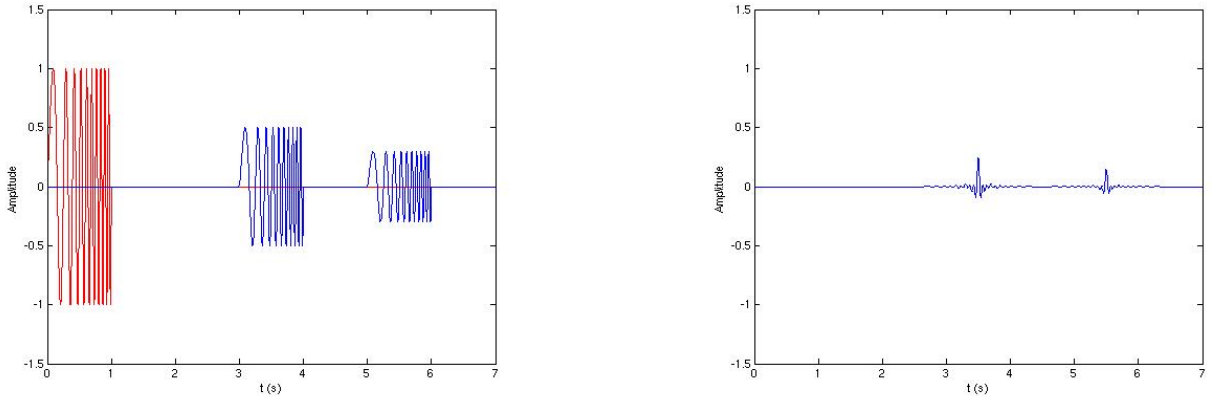

(a) signal before matched filtering (b) signal after matched filtering

Figure 7.1: Images from wikipedia [27].

Also, since the power is concentrated in the main lobe of the cardinal sine instead of being spread out on the pulse, it is easier to recognize the echo amid the noise.

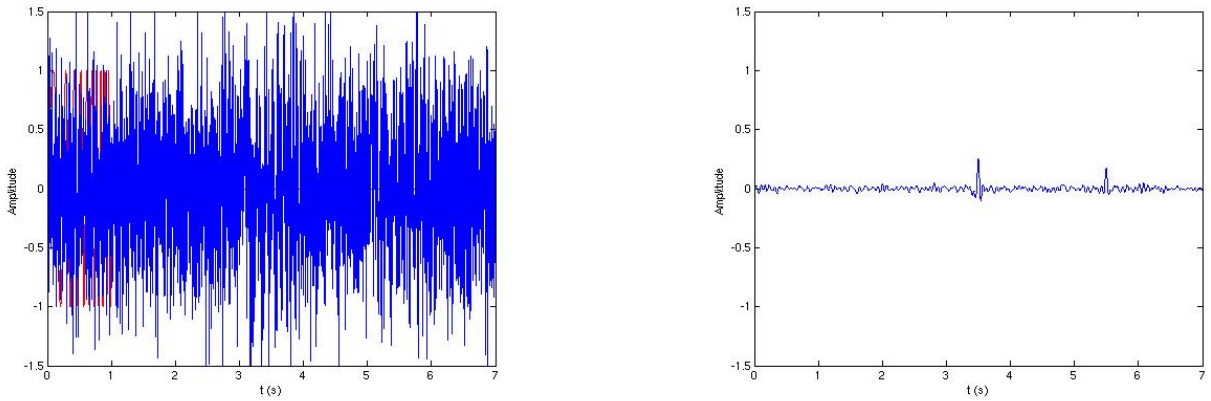

(a) signal in noise before matched filtering (b) signal in noise after matched filtering

Figure 7.2: Images from Wikipedia [27].

This gain on the SNR is computed as $T\,B$, where T is the length of the pulse and B the bandwidth of the signal.
As we can see, when we increase the bandwidth of our signal, it increases the gain of the pulse compression, but it also increases the average noise power (defined as kT_sB). Thus, varying the bandwidth size does not modify the SNR.
The circuitry for larger bandwidth tends to be more expensive, so a small bandwidth of 10 MHz is chosen, given our limited needs in terms of range resolution.
The range resolution depends on the bandwidth, improving as the bandwidth gets larger. The depth resolution is defined as

$$\Delta R = \frac{c}{2B} \tag{7.5}$$

For a bandwidth of 10 MHz, we get a range resolution of 15 m. This is largely sufficient as the probability of multiples debris being less than 15 m apart from each other is very low in space. Also, this should be precise enough to track the debris. Once the satellite that will remove the object will be close enough to the debris, it will be able to change its way of tracking the object to its own tracking system (probably optical) to approach and capture its target.

Since the radar we use is pulsed, we do not emit continuously, but a possibility is to have the signal generator running at all times, but have the power amplifier which connects to the emitting antenna function intermittently. This way, we can split the signal from the generator; on one side it would reach the power amplifier to be emitted, and on the other side it can be used to be compared with the received signals in order to give information on the timing compared to the emitted wave and thus detect the position of the target, as illustrated in Figure 7.3.

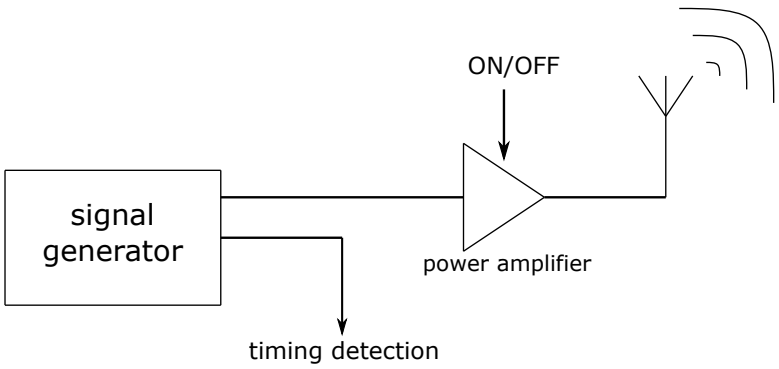

Figure 7.3: illustration of the generated signal splitting

In order to compare these signals, two methods exist, and the choice of which one to use has not been made yet. The first one consists in filters with an impulse response close to the time-reversed transmitted signal. The second technique is the numerical correlation by using the Fourier transform of the signals.

7.2.2 Coherent integration

Coherent integration improves the detection probability by summing following pulses before checking the threshold. Since the noise is white (equal intensities at different frequencies) and Gaussian, it will not sum constructively as we add up multiple pulses, but if there is a reflection from an object in the received signals, its additions will be constructive and a peak should appear above the noise. The peak created by the echo should be greater as we integrate more pulses.

The effect on the SNR is a multiplication by the number of pulses integrated N. Since we are working in dB, we can add to our SNR a term of $10 \log_{10} N$.

The number of pulses we can integrate usefully for a single target depends on the time this target stays in the "field of view" of the radar, and thus on the target's velocity relative to the radar. If too many pulses are integrated, the echos of multiple targets might be integrated together and might produce confusing results. This could create a false positive at a certain spot, or a preceding object's echo might mix with a following one which would be in the same range, but passing through the radar field at a later time.
In order to know how many pulses we should integrate, an approximate/average value of the debris' speed in the geosynchronous orbit is needed. The speed of debris in the Low Earth Orbit is around 7 km/s. As we do not have any information regarding the velocity at the GEO, we will use the same value in our computations. This is an important factor in determining how many pulses we can add up and the SNR calculation might be less accurate because of this lack of information. The number of pulses that could be integrated also depends on the width of the radar's beam and the distance between the radar and the object. In the worst case scenario to have the lowest number of pulses that could be integrated, we take the closest an object could be seen, the limit here being the blank zone : 50 km. Since the beamwidth of the antenna is 7.8°, this gives an arc of length $\alpha d = \frac{7.8*\pi}{180} * 50 \approx 6.8$ km. With a debris speed of 7 km/s, supposing the debris follows the arc perfectly, it would thus stay visible to the radar for 0.97 seconds. The pulse period repetition being 2.33 ms long (set by the maximum distance surveyed), we find it is possible to integrate 416 consecutive pulses, adding 26.19 dB to our signal-to-noise ratio.

7.3 ROC

The Receiver Operating Characteristic (ROC) for a radar is a graph plotting the probability of detection against the false positive rate, with respect to the SNR needed to achieve such odds. As we strive for a low false alarm rate and a great detection rate, a high SNR is needed.

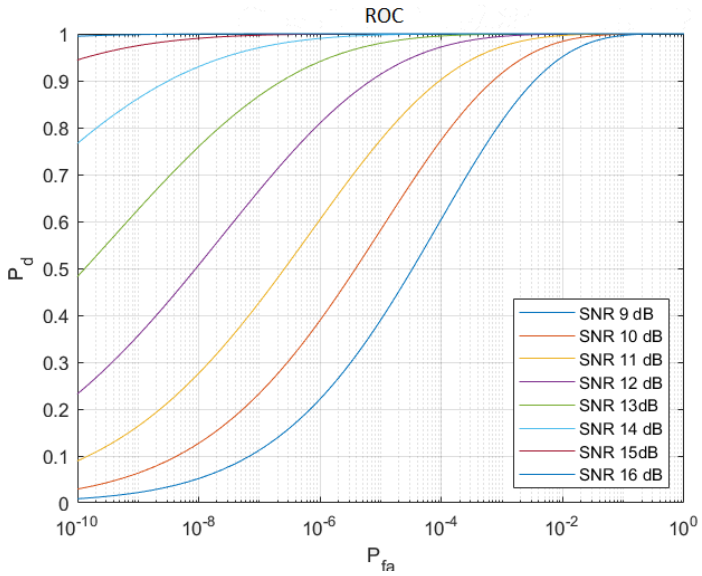

Figure 7.4: Receiver operating characteristic

A good false alarm probability is 10^{-3}, and a detection probability of 0.9. To reach these values, an SNR of approximately 10 dB would be needed.

An Excel spreadsheet was made with all of these data and variables, allowing one to change easily some parameter and seeing its impact on other parameters and on the capabilities of the radar.

With this, we can define boundaries on the detection capabilities of radar :
Firstly, the radar cross section of the smallest object we can detect, expressed as as sphere of a particular radius - which would correspond to a cube with a geometrical section approximately π times smaller. Secondly, the maximum possible distance for the detection for a specific size of object.

Our objective for the radar was to detect cubes that have a side length of the wavelength (in this case 6 cm). Using the average RCS, we find the following curve for the signal-to-noise ratio :

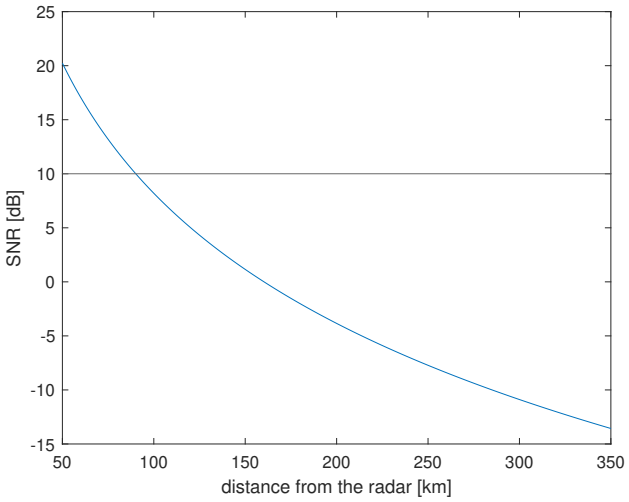

Figure 7.5: SNR evolution with distance from the radar, with the RCS of a cube with a side length of 6 cm.

As long as the curve is above the horizontal line at 10 dB, the target is detected by the radar. A target with a higher radar cross section would move the curve upward.

Since the limit set for a correct detection is set at 10 dB, we notice from figure 7.5 that we can observe a cube of that size up to 90 km. We must not forget the blank zone preventing us from seeing before 50 km from the radar. Thus we can actually detect objects of such size for 40 km. Above these 90 km, the SNR would be lower than 10 dB, and the debris will not be detected by the radar. Of course, this is for the average of the RCS of the cube; depending on its orientation in relation to the radar, it might be visible for a longer or shorter distance.

It is also interesting to determine the maximal distance from which we can see object of different sizes. To compare the objects, we use spheres, since they keep the same cross section from any angle observed. Again, we cannot observe anything before 50 km, so the smaller objects (the part of the curve beneath the horizontal line) won't be visible at all for our radar.

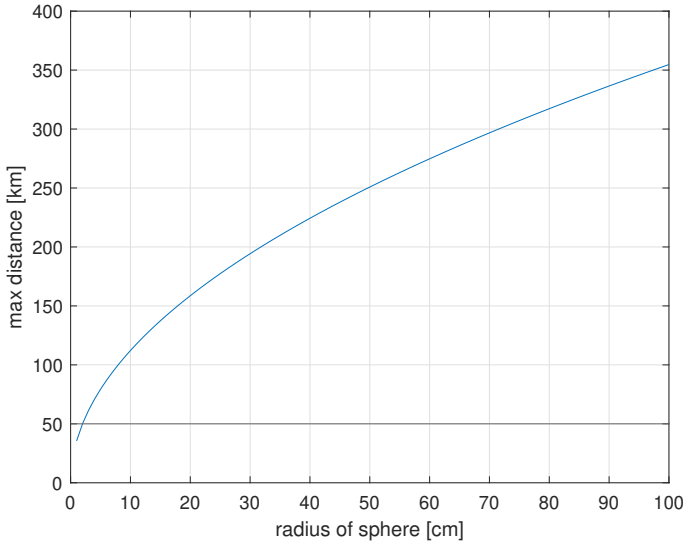

Figure 7.6: graph of the distance spheres of varying radius can be seen. Theses spheres have the same RCS as cubes with a geometrical cross-section π times smaller than the spheres'.

As we can see from Figure 7.6, sphere with a radius lower than 2cm are not visible to our radar in any case. We can also observe the minimum size of object that can be seen up to the end of the geostationary orbit, they must have the same RCS as a sphere with a radius just under 1 m, which corresponds to quite large debris.

CHAPTER 8

CONCLUSION

Detection, tracking and cataloguing debris in the geostationary orbit is a task that should be tackled as soon as possible. A satellite-mounted radar could be a great means of detecting these debris.

In order to survey the whole geostationary belt, the radar will fly on an orbit 150 km lower than the GEO center. Since this lower orbit have a shorter revolution than the geostationary orbit, the radar will move at a different speed than on the GEO and will be able to scan the 360° of the belt around the globe. To scan in the perpendicular direction, beamforming will be used with an array of antennas, allowing one to steer the beam and to scan 'perpendicularly' to the orbit.

The pulse frequency-modulated radar, with a pulse length of 333 μs, will have a blank zone of 50 km where no debris will be visible and will scan up to 350 km in depth. Powered by 3 m^2 of solar panels supplying around 500 W to the radar, the power per pulse is at 3500 W.

The final design of the antenna array features 16 antennas with a squared cosine width distribution. Spaced by 56 mm, the array has a maximum gain of 30.3 dB and an mainbeam of 7.8°, an S-parameter lower than -10 dB in the 10 MHz around 5 GHz, the bandwidth of the radar.

The RCS response of a square plate with a side of a few wavelengths has been computed and discussed upon. While the average RCS of a cube has been measured at 0.0131 m^2 at 5 GHz, the response of the plate depends a lot on the frequency as well as the on angle of incidence of the electromagnetic wave. As we rise in frequency, the overall RCS response increases too but becomes more concentrated around the normal to the plate, that is when the plate is facing perfectly the radar - which does not occur more often than other angles; the plate becomes harder to detect at higher angles, and thus the overall probability to detect the debris may decrease. Also, if we wish to keep a certain effective aperture A_e, as we increase the frequency, it would require a higher number of elements and thus channels in the array, which would make the system more complex, costly and more power-hungry. The choice of frequency must therefore be carefully considered.
A constant has been found to approximate the average RCS response of a plate which side length is close to the wavelength : $9/(4\pi) \cdot A$, where A is the surface of the plate. While this constant is not accurate for lower and much higher frequencies, an analytical solution was developed for lower frequencies and a curve fitting was done to find a function matching the RCS response for higher frequencies.

Finally, the SNR of the radar for different situations is computed. In order to improve it, we have considered pulse compression by using a matched filter on the returning wave and coherent integration to add up adjacent returning pulses. For a detection probability of 0.9 and a constant false alarm rate at 10^{-3}, a SNR equal or greater than 10 dB is required. For the cube of which the average RCS was computed, this means the radar will be able to detect it up to 90 km. The size of object possible to detect up to the end of the geostationary orbit, 350 km from the radar, needs to have at least the same RCS response as a sphere with a radius of 1 m, which seems too demanding if the size of the antenna is not increased.

One of the most important and impactful choices made in this thesis is what frequency to work at. It has a strong impact on the SNR, wheter we use the constant gain or constant effective aperture formula, but is also strongly influences the RCS in multiple ways. A higher frequency will increase the maximum RCS response, but will make the plate less visible from other angle than when the normal to the plate is aligned with the radar. We were looking for a good compromise between the RCS response, the visibility at multiple angles, the direct influence on the SNR and the dimensioning of the antenna, which overall size is proportional to the wavelength of the radar. There is also the increase of the number of channels needed as we increase the frequency used. This will affect the complexity of the system, especially for the beamforming needed in order to scan vertically. Using 5 GHz seems to fit this compromise, but it could be feasible to work at a higher frequency.

In perspective, the efficiency of the radar could still be improved, as it is for now limited to 90 km for the detection of target the size of its wavelength, 6 cm. Another avenue for improvement would be the cell resolution, by making the antenna and the array more directive. Possibly, the maximum gain of said array could be increased even higher in order to improve the SNR and thus the range of small debris detecting of the radar. It could be interesting to use a MIMO radar which would have a large virtual array from a much lower number of physical antennas, in order to improve the spatial resolution. The difficulty of implementing such a radar would be the deployment of the array of antennas, as either the receiving or emitting antennas would need a significant spacing between elements for the virtual array to be large.

BIBLIOGRAPHY

[1] Dailymail, "Dailymail : huge cloud of space junk created by russia's anti-satellite test." [online] Available at: https://www.dailymail.co.uk/sciencetech/article-10229955/Shocking-visualisations-reveal-huge-cloud-space-junk-created-Russias-anti\-satellite-test.html [Accessed 5 April 2022].

[2] ESA, "Annual space environment report." [Online] Available: https://www.sdo.esoc.esa.int/environment_report/Space_Environment_Report_latest.pdf [accessed on 19 May 2022], February 2022.

[3] ISO, "Standard space systems — space debris mitigation requirements, iso 4113:2019." [online] Available at: https://www.iso.org/standard/72383.html [Accessed 23 April 2022].

[4] ESA, "Space situational awareness overview." [Online] Available: https://www.esa.int/Safety_Security/SSA_Programme_overview [accessed on 19 May 2022].

[5] Lockheed-Martin, "Space fence," July 2021. [Online] Available: https://www.lockheedmartin.com/en-us/products/space-fence.html.

[6] F. I. for High Frequency Physics and R. T. FHR, "Space observation radar tira." [Online] Available: https://www.fhr.fraunhofer.de/en/the-institute/technical-equipment/Space-observation-radar-TIRA.html [accessed on 15 May 2022].

[7] Wikipedia, "Graves space surveillance system." [Online] Available: https://en.wikipedia.org/wiki/Graves_%28system%29 [accessed on 15 May 2022.

[8] ESA, "New laser station lights the way to debris reduction." [Online] Available: https://www.esa.int/Safety_Security/Space_Debris/New_laser_station_lights_the_way_to_debris_reduction [accessed on 11 May 2022.

[9] MIT, "Space surveillance telescope." [online] Available at: https://www.ll.mit.edu/r-d/projects/space-surveillance-telescope [Accessed 7 April 2022].

[10] G. L. Somma, P. Bowman, M. Dayas, S. Walker, S. Reid, and C. Brunskill, "Reusing existing infrastructure to identify and monitor resident space objects," 2021.

[11] P. W. Kelly, R. Bevilacqua, L. Mazal, and R. S. Erwin, "Tugsat: removing space debris from geostationary orbits using solar sails," *Journal of Spacecraft and Rockets*, vol. 55, no. 2, pp. 437–450, 2018.

[12] S. Kitamura, Y. Hayakawa, and S. Kawamoto, "A reorbiter for large geo debris objects using ion beam irradiation," *Acta Astronautica*, vol. 94, no. 2, pp. 725–735, 2014.

[13] J. Missel and D. Mortari, "Removing space debris through sequential captures and ejections," *Journal of Guidance, Control, and Dynamics*, vol. 36, no. 3, pp. 743–752, 2013.

[14] C. Blackerby, A. Okamoto, K. Fujimoto, N. Okada, J. L. Forshaw, and J. Auburn, "Elsa-d: An in-orbit end-of-life demonstration mission," in *69th International Astronautical Congress*, 2018.

[15] T. Hitchens, "China's sj-21 'tugs' dead satellite out of geo belt." [online] Breaking Defense. Available at: `https://breakingdefense.com/2022/01/chinas-sj-21-tugs-dead-satellite-out-of-geo-belt-trackers/` [Accessed 11 May 2022].

[16] R. Biesbroek, S. Aziz, A. Wolahan, S.-f. Cipolla, M. Richard-Noca, and L. Piguet, "The clearspace-1 mission: Esa and clearspace team up to remove debris," in *Proc. 8th Eur. Conf. Sp. Debris*, pp. 1–3, 2021.

[17] D. Forbes and S. Hubbard, "Solar-cell-efficiency enhancement using nanostructures." [online] Spie. Available at: `https://spie.org/news/3124-solar-cell-efficiency-enhancement-using-nanostructures?SSO=1` [Accessed 15 April 2022].

[18] D. C. Jordan and S. R. Kurtz, "Photovoltaic degradation rates—an analytical review," *Progress in photovoltaics: Research and Applications*, vol. 21, no. 1, pp. 12–29, 2013.

[19] M. Bekemans, E. De Jaeger, J. Bou Saada, and J. Ghoy, "Electronique de l'energie." Université Catholique de Louvain, 2019.

[20] M. I. Skolnik, "Radar handbook," 1970.

[21] C. Craeye, "Lelec2910 : Antenna and propagation." Chapter 4, page 10.

[22] H. Forstén, "Mimo radar antenna arrays." [online] Available at: `https://hforsten.com/mimo-radar-antenna-arrays.html` [Accessed 29 May 2022].

[23] C. Craeye, "Lelec2350 : Electromagnetic waves : Physical optics." Chapter 8 to 14, page 37.

[24] C. A. Balanis, *Antenna theory: analysis and design*. John wiley & sons, 2015.

[25] Pasternack, "Microstrip patch antenna calculator." [online] Pasternack. Available at: `https://www.pasternack.com/t-calculator-microstrip-ant.aspx` [Accessed 18 April 2022].

[26] M. L. Library, "Introduction to radar systems." [online] Available at: `https://www.ll.mit.edu/outreach/radar-introduction-radar-systems-online-course` [Accessed 1 December 2021].

[27] Wikipedia, "Pulse compression." [online] Available at: `https://en.wikipedia.org/wiki/Pulse_compression` [Accessed 6 April 2022].

UNIVERSITÉ CATHOLIQUE DE LOUVAIN
École polytechnique de Louvain
Rue Archimède, 1 bte L6.11.01, 1348 Louvain-la-Neuve, Belgique | **www.uclouvain.be/epl**